Originally published as:

1 **Consistency between sun-induced chlorophyll fluorescence and gross primary**

2 **production of vegetation in North America**

3 Yao Zhang[1], Xiangming Xiao[1,2,*], Cui Jin[1], Jinwei Dong[1], Sha Zhou[3], Pradeep Wagle[1], Joanna Joiner[4], Luis

4 Guanter[5], Yongguang Zhang[6], Geli Zhang[1], Yuanwei Qin[1], Jie Wang[1], Berrien Moore III[7]

5

6 [1]Department of Microbiology and Plant Biology, Center for Spatial Analysis, University of Oklahoma, Norman,

7 OK 73019, USA; [2]Institute of Biodiversity Science, Fudan University, Shanghai, 200433, China; [3]State Key

8 Laboratory of Hydroscience and Engineering, Department of Hydraulic Engineering, Tsinghua University, Beijing,

9 China; [4]NASA Goddard Space Flight Center, Greenbelt, MD, USA; [5]Helmholtz Centre Potsdam, German

10 Research Center for Geosciences (GFZ), Telegrafenberg A17, 14473 Potsdam, Germany; [6]Jiangsu Provincial Key

11 Laboratory of Geographic Information Science and Technology, International Institute for Earth System Sciences,

12 Nanjing University, 210023 Nanjing, China; [7]College of Atmospheric and Geographic Sciences, University of

13 Oklahoma, Norman, OK 73019, USA

14

15 *Corresponding Author: Prof. Xiangming Xiao (xiangming.xiao@ou.edu)

16

20

Abstract

Accurate estimation of the gross primary production (GPP) of terrestrial ecosystems is vital for a better understanding of the spatial-temporal patterns of the global carbon cycle. In this study, we estimate GPP in North America (NA) using the satellite-based Vegetation Photosynthesis Model (VPM), MODIS images at 8-day temporal and 500 m spatial resolutions, and NCEP-NARR (National Center for Environmental Prediction-North America Regional Reanalysis) climate data. The simulated GPP (GPP_{VPM}) agrees well with the flux tower derived GPP (GPP_{EC}) at 39 AmeriFlux sites (155 site-years). The GPP_{VPM} in 2010 is spatially aggregated to 0.5 by $0.5°$ grid cells and then compared with sun-induced chlorophyll fluorescence (SIF) data from Global Ozone Monitoring Instrument 2 (GOME-2), which is directly related to vegetation photosynthesis. Spatial distribution and seasonal dynamics of GPP_{VPM} and GOME-2 SIF show good consistency. At the biome scale, the relationship between GPP_{VPM} and SIF shows strong linear relationships ($R^2 > 0.95$) and small variations in slopes ($4.60 - 5.55$ g C m^{-2} day^{-1} / mW m^{-2} nm^{-1} sr^{-1}). The total annual GPP_{VPM} in NA in 2010 is approximately 13.53 Pg C $year^{-1}$, which accounts for ~11.0% of the global terrestrial GPP and is within the range of annual GPP estimates from six other process-based and data-driven models ($11.35 - 22.23$ Pg C $year^{-1}$). Among the seven models, some models did not capture the spatial pattern of GOME-2 SIF data at annual scale, especially in Midwest cropland region. The results from this study demonstrate the reliable performance of VPM at the continental scale, and the potential of SIF data being used as a benchmark to compare with GPP models.

1. Introduction

45   Carbon dioxide fixed through photosynthesis by terrestrial vegetation is known as gross

46   primary production (GPP) at the ecosystem level. Increased carbon uptake during the past

47   decades helped offset growing CO_2 emissions from fossil fuel burning and land cover change

48   and mitigate the increase of atmospheric CO_2 concentration and global climate warming

49   (Ballantyne et al. 2012). A variety of approaches have been used to estimate GPP of terrestrial

50   ecosystems, and they can be grouped into four categories: 1) process-based GPP models; 2)

51   satellite-based production efficiency models (PEM); 3) data-driven GPP models upscaled from

52   eddy covariance data; and 4) models based on sun-induced chlorophyll fluorescence (SIF) (Fig.

53   1). However, large uncertainty still remains regarding the spatial distribution and seasonal

54   dynamics of GPP, which limits our capability to address scientific questions related to the

55   increasing seasonal amplitude and interannual variation of atmospheric CO_2 (Graven et al.

56   2013; Poulter et al. 2014; Forkel et al. 2016). An accurate estimation of GPP at regional and

57   global scales is essential for a better understanding of the underlying mechanisms of

58   ecosystem-climate interactions and ecosystem response to extreme climate events, such as

59   drought, heat wave, and flood, etc. (Beer et al. 2010; Yu et al. 2013; Zhang et al. 2016).

60   Many process-based biogeochemical models employ the enzyme kinetics theory, most

61   well-known as encapsulated by Farquhar et al. (1980) and its modification for C4 plants

62   (Collatz et al. 1992). Some process-based models employ the light-use-efficiency (LUE)

63   concept to estimate GPP (Zeng et al. 2005). These models also take multiple ecological

64   processes into consideration so that they can be coupled with general circulation models

65   (GCMs) to predict feedbacks related to the global warming and CO_2 fertilization (Booth et al.

66   2012; Keenan et al. 2012; Piao et al. 2013; Xia et al. 2014). However, these models are often

67   run at coarse spatial resolution and the simulation results vary enormously even with the same

68   set of meteorological input datasets (Coops et al. 2009).

69   The remote sensing based PEMs estimate GPP as the product of the energy absorbed by

70   plants (absorbed photosynthetically active radiation, APAR) and LUE that converts energy to

71   carbon fixed during the photosynthesis process (Monteith 1972). These models can be further

72   divided into two subcategories (Dong et al. 2015a; Xiao et al. 2004a). The $FPAR_{canopy}$ based

73   models, including the Carnegie Ames Stanford Approach (CASA) (Potter et al. 1993), the

74   MODIS GPP algorithm (Photosynthesis, PSN) (Running et al. 2004; Zhao et al. 2005), and the

75   EC-LUE model (Yuan et al. 2007), use the radiation absorbed by vegetation canopy. The

76   $FPAR_{chl/green}$ based models use radiation absorbed by chlorophyll or green leaves and

77   include the Vegetation Photosynthesis Model (VPM) (Xiao et al. 2004a; Xiao et al. 2004b),

78   Greenness and Radiation (GR) model (Gitelson et al. 2006), and the Vegetation Index (VI)

79   model (Wu et al. 2010b).

80   The eddy covariance (EC) technique provides estimates of GPP by partitioning measured

81   net ecosystem CO_2 exchange (NEE) between land and the atmosphere into GPP and ecosystem

82   respiration (R_e) (Baldocchi et al. 2001). Over the past decades, the EC technique has been

83   widely applied to measure NEE of various biome types throughout the world, and a large

84   amount of GPP data (GPP$_{EC}$) has been accumulated (Baldocchi 2014; Baldocchi et al. 2001).

85   A number of statistical models have been developed to upscale GPP$_{EC}$ from individual sites to

86   the regional scales (Jung et al. 2009; Jung et al. 2011; Xiao et al. 2010; Xiao et al. 2014; Yang

87   et al. 2007). These algorithms, such as model tree ensembles (MTE) or regression tree

88   approaches, build a series of rules through data mining that relate *in situ* flux observations to

89   satellite-based indices and climate data.

90   Solar-induced chlorophyll fluorescence (SIF), a byproduct of the vegetation photosynthesis

91   process, has been recently retrieved using multiple satellite platforms/instruments such as the

92   Greenhouse gases Observing SATellite (GOSAT) (Frankenberg et al. 2011; Guanter et al. 2012;

93   Joiner et al. 2012; Joiner et al. 2011), the Global Ozone Monitoring Instrument 2 (GOME-2)

94   (Joiner et al. 2013), and the Orbiting Carbon Observatory-2 (OCO-2) (Frankenberg et al. 2014).

95   Recent field studies and theory suggest that SIF contains information from both APAR and

96   LUE that is complementary to vegetation indices such as the normalized difference vegetation

97   index (NDVI) (Guanter et al. 2013; Rossini et al. 2015; Yang et al. 2015). A simple regression

98   model based on space-borne SIF has been developed to estimate cropland GPP (Guanter et al.

99   2014). Zhang et al. (2014) have also shown the potential of SIF data to improve carbon cycle

100   models and provide accurate projections of agricultural productivity (Guan et al. 2015).

101
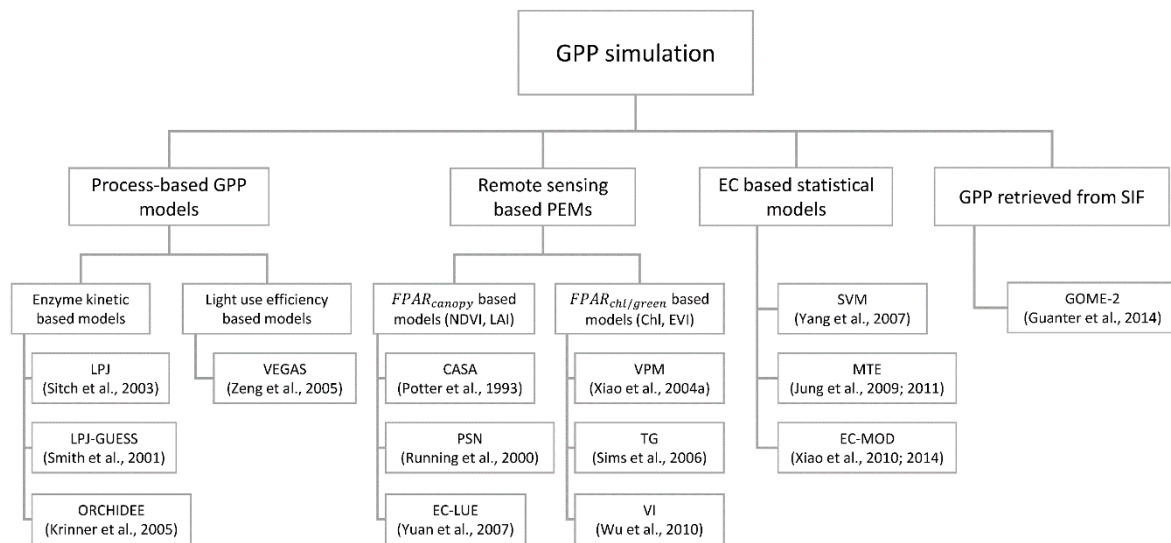
Fig. 1. A list of different approaches and models (as examples) to estimate gross primary production (GPP) of vegetation.

Over the past several years, a number of studies have run the VPM with *in situ* climate data at various eddy flux tower sites. The resulting GPP$_{VPM}$ was evaluated with GPP$_{EC}$ at different ecosystem types, including forests (Xiao et al. 2004a; 2004b; 2005), croplands (Kalfas et al. 2011; Wagle et al. 2015), savannas (Jin et al. 2013), and grasslands (He et al. 2014; Wagle et al. 2014). Wu et al. (2010a) compared GPP from four models driven by remotely sensed data at the Harvard forest site and found that VPM performed best in terms of capturing the seasonal dynamics of GPP. Yuan et al. (2014) compared seven LUE based models at 157 eddy flux sites and showed that VPM had a moderate rank of performance. Dong et al. (2015a) used four EVI-based models to estimate GPP of grasslands and croplands under normal and severe drought conditions, and reported that VPM performed better than other models in capturing the impacts of drought on GPP. This was mostly because VPM uses Land Surface Water Index (LSWI) that is sensitive to water stress (Wagle et al. 2014; 2015), while the other three models lack a water

118   stress scalar. Recently, simulations of VPM on the regional scale, driven by regional climate

119   data, have been carried out in the Tibetan Plateau (He et al. 2014) and China (Chen et al. 2014),

120   where only limited GPP_{EC} data are available for model calibration and validation.

121   In this study, we aim to assess the feasibility and performance of the VPM model in

122   estimating GPP across North America (NA) and explore the relationship between SIF and

123   GPP_{VPM} at continental scale. The selection of the NA as study area is based on two facts: (1)

124   large uncertainties exist in the GPP estimates from various models (ranging from 12.2 to 32.9

125   Pg C year^{-1}) (Huntzinger et al. 2012); and (2) a large number of eddy flux sites are available in

126   NA, which provides an opportunity for a thorough validation. The specific objectives of this

127   study are to: (1) implement the VPM simulation at the continental scale over NA; (2) evaluate

128   the performance of VPM at individual sites using GPP_{EC} data from 39 flux tower sites (155

129   site-years); (3) compare GPP_{VPM} with GOME-2 SIF data at 0.5° (latitude/longitude) resolution

130   across NA; and (4) use of GOME-2 SIF as a reference to compare with GPP estimates from

131   other six models. In this paper, we report (1) multi-year GPP_{VPM} and GPP_{EC} at individual flux

132   tower sites, dependent upon availability of GPP_{EC} data, and (2) GPP_{VPM} in 2010 across NA.

133   **2.   Materials and Method**

134   **2.1. Regional datasets for VPM simulations across North America**

135   **2.1.1. Climate data**

136   The VPM model uses photosynthetically active radiation (PAR) and temperature data as

137   climate input data. We use the National Center for Environmental Prediction-North America

138   Regional Reanalysis (NCEP-NARR) datasets (Mesinger et al. 2006) for 2000-2014. The

139   original three hourly data are first aggregated into 8-day averages to match the temporal

140   resolution of MODIS vegetation indices. The day-time mean air temperature is obtained by

141   averaging the temperature between 6 am to 6 pm local time. Zhao et al. (2006) reported that

142   the NCEP-NARR product overestimates the surface shortwave radiation when comparing with

143   the *in situ* observation at the flux tower sites. Jin et al. (2015) also compared the NCEP-NARR

144   radiation data with *in situ* radiation measurements at 37 AmeriFlux sites and reported a bias

145   correction factor of 0.8. In this study, we applied this factor to adjust the radiation data.

146   In order to run VPM at a 500 m spatial resolution, we use a non-linear spatial interpolation

147   method (Zhao et al. 2005) to downscale the NCEP-NARR radiation and temperature dataset

148   from the spatial resolution of 0.25°×0.25° to 500-m. It uses a fourth power of a cosine function

149   and adopts the weighted distance from the nearest four grid cells to calculate a value for each

150   output pixel at MODIS resolution. The distance factor (D_i) for the four nearby grid cells can

151   be calculated as follows:

152    $$D_i = cos^4\left(\frac{\pi}{2} \times \left(\frac{d_i}{d_{max}}\right)\right) \qquad i = 1,2,3,4 \qquad (1)$$

153   where d_i and d_{max} indicate the distance between the center of the 500 m MODIS pixel and

154   each of the four vertex grid cells from NCEP-NARR data, and the maximum distance between

155   the four vertex NCEP-NARR grid cells, respectively. For each MODIS pixel, the weight from

156   the four surrounding NCEP-NARR grid cells can be calculated as:

157    $$W_i = \frac{D_i}{\sum_{i=1}^{4} D_i} \qquad (2)$$

158   The final value for each interpolated MODIS pixel (V) can be expressed as a weighted

159   average:

$$V = \sum_{i=1}^{4} (W_i * V_i) \qquad (3)$$

161   where V_i is the value for the four surrounding grid cell values of NCEP-NARR data.

2.1.2. MODIS data

2.1.2.1. MODIS surface reflectance and vegetation indices

164   The MODIS MOD09A1 surface reflectance product (500 m spatial resolution and 8-day

165   temporal resolution) is used to calculate the enhanced vegetation index (EVI) (Huete et al. 2002)

166   and LSWI as inputs to the VPM. LSWI is calculated as the normalized difference between NIR

167   (0.78-0.89μm) and SWIR (1.58-1.75μm) and is sensitive to water content. Therefore, LSWI is

168   a good indicator of water stress from the vegetation canopy and soil background (Xiao et al.

169   2002). These two indices are calculated as follows:

$$EVI = 2.5 \times \frac{\rho_{nir} - \rho_{red}}{\rho_{nir} + (6 \times \rho_{red} - 7.5 \times \rho_{blue}) + 1} \qquad (4)$$

$$LSWI = \frac{\rho_{nir} - \rho_{swir}}{\rho_{nir} + \rho_{swir}} \qquad (5)$$

172   A temporal gap-fill algorithm is applied to the EVI time series data. The data quality is

173   checked using the quality flag layer, and those observations not affected by cloud and

174   climatological aerosols are considered 'GOOD' quality (MOD35 cloud = 'clear'; aerosol

175   quantity = 'low' or 'average'). Each pixel is temporally linearly interpolated using only good-

176   quality EVI observations within each year. A Savitzky–Golay filter is then applied to each pixel

177   to eliminate high frequency noise (Chen et al. 2004). If a pixel has fewer than three out of 46

178   good observations for one year, the original data (no gap-filled) are used. Fortunately, this

9

179 happens only for < 0.5% of the total pixels and the majority of those are in less productive,

180 boreal areas.

2.1.2.2. MODIS land cover data

182 The MODIS MCD12Q1 land cover product at 500-m spatial resolution (Friedl et al. 2010)

183 includes annual land cover types from 2001 to 2013. We use MCD12Q1 data in 2001 to

184 represent year 2000, and MDD12Q1 data in 2013 to represent year 2014, which allows us to

185 have a full time series of land cover types for 2000-2014. The IGBP land cover classification

186 scheme in the dataset is used to provide biome specific information for the VPM. A lookup-

187 table (LUT) is used to get the essential parameters including maximum LUE as well as the

188 maximum, minimum, and optimum temperatures for vegetation photosynthesis (see Appendix

189 Table A1).

190 In order to investigate the relationship between GPP$_{VPM}$ and SIF (0.5° latitude and

191 longitude resolution) in different vegetation/biome types, we also aggregate the original 500 m

192 land cover data to 0.5° grid cells using the following procedure. The original IGBP land cover

193 data are first merged and reprojected onto the longitude-latitude projection with the original

194 spatial resolution. We calculate the frequency (number of 500 m pixels) of individual

195 vegetation types within a 0.5° × 0.5° grid cell. Then, for each 0.5° × 0.5° grid cell, if one

196 vegetation type is dominant (> 75% of the grid cell), this grid cell is assigned that vegetation

197 type; if no land cover type is dominant, the grid cell is not assigned a type.

198 **2.1.2.3. MODIS land surface temperature data**

199   The MODIS MYD11A2 land surface temperature dataset is used to derive the thermal

200 growing season and eliminate the snow cover period, which avoids the effect of snow cover in

201 retrieving the yearly maximum LSWI. The MYD11A2 data set is chosen because it provides

202 observations at 1:30 am, which is close to the daily minimum temperature. For each pixel each

203 year, the thermal growing season is defined using the nighttime land surface temperature (Dong

204 et al. 2015b). Once three consecutive 8-day's in the spring have nighttime temperatures above

205 5℃, the thermal growing season begins; when three consecutive 8-day's in the fall have

206 nighttime temperatures below 10℃, the thermal growing season ends. A detailed application

207 of this temperature-based phenology was recently reported (Zhang et al. 2015).

208 **2.2. Datasets used to evaluate and compare VPM simulations across North America**

209 **2.2.1. CO_2 eddy flux data from AmeriFlux tower sites**

210   CO_2 flux data from 39 AmeriFlux sites are downloaded from the AmeriFlux data portal

211 (http://ameriflux.ornl.gov/). These flux sites cover most of the major biomes in NA (DBF, ENF,

212 MF, GRA, CRO, CSH, OSH, WET and WSA) (Table 1). The 8-day level-4 gap-filled flux data

213 with the Marginal Distribution Sampling (MDS) method is used (Reichstein et al. 2005). GPP_{EC}

214 estimates from individual sites are used to evaluate GPP_{VPM}.

215 **2.2.2. Solar-induced chlorophyll fluorescence (SIF) data from GOME-2**

216   The latest version (v26) of monthly SIF data from the GOME-2 instrument onboard

217 Eumetsat's MetOp-A satellite is used in this study and available to the public at http://acdb-

218 ext.gsfc.nasa.gov/People/Joiner/my_gifs/GOME_F/GOME-F.htm (Joiner et al. 2014). GOME-

219 2 captures earth radiation in the range from ~600 to 800 nm with a spectral resolution of ~0.5

220 nm at a nominal nadir footprint of 40×80 km^2 in the nominal observing configuration.

221 Wavelengths around 740 nm at the far-red peak of the SIF emission are used for SIF retrievals

222 with a principal component analysis approach to account for atmospheric absorption. The

223 results are then quality-controlled (e.g., heavily cloud contaminated data removed) and

224 aggregated to monthly means at $0.5° \times 0.5°$ spatial resolution (Joiner et al. 2013). In this study,

225 we use GOME-2 SIF data for the period from January 2010 to February 2011.

226 **2.2.3. GPP data from other six models**

227   The GPP data from the four process-based models (LPJ, LPJ-GUESS, ORCHIDEE, and

228 VEGAS) are part of the TRENDY projects (Sitch et al., 2008), which intended to compare

229 trends in net land-atmosphere carbon exchange over the period 1980 – 2010 (Table 3). These

230 four models, driven by the CRU+NCEP climate data and global annual atmospheric CO_2, are

231 chosen because they have different algorithms to simulate GPP at $0.5°\times0.5°$ spatial resolution.

232   Another two models involved in the comparison are the MPI-BGC and MODIS PSN. The

233 MPI-BGC estimates GPP by upscaling global CO_2 flux observations using a Model Tree

234 Ensemble approach (Jung et al. 2009). MODIS PSN employs a production-efficiency approach

235 and uses the MODIS fraction of photosynthetically active radiation product (MOD15A2) and

236 meteorological data (Running et al. 2004). The C55 version of MODIS PSN product

237 (MOD17A2 C55) is used.

2.3. A brief description of the Vegetation Photosynthesis Model (VPM)

The satellite-based VPM (Xiao et al., 2004a, b) uses the product of light use efficiency (LUE, ε_g), and absorbed photosynthetically active radiation by chlorophyll ($APAR_{chl}$) to estimate GPP as follows (Fig. 2):

$$GPP = \varepsilon_g \times APAR_{chl} \qquad (6)$$

VPM uses the fraction of absorbed photosynthetic active radiation by chlorophyll ($fAPAR_{chl}$) to estimate $APAR_{chl}$. The $fAPAR_{chl}$ is estimated from a linear function of EVI where the coefficient α is set to be 1.0 (Xiao et al. 2004a).

$$APAR_{chl} = fAPAR_{chl} \times PAR \qquad (7)$$

$$fAPAR_{chl} = \alpha \times EVI \qquad (8)$$

The light-use-efficiency (ε_g) in the VPM is a down-regulation of maximum LUE (ε_0) by temperature (T_{scalar}) and water stress limitation (W_{scalar}) on photosynthesis as follows:

$$\varepsilon_g = \varepsilon_0 \times T_{scalar} \times W_{scalar} \qquad (9)$$

ε_0 is a biome-specific parameter and differs for C3 and C4 plants. The ε_0 values are obtained from a lookup-table (LUT) using the MODIS land cover data. T_{scalar} is estimated from the equation used in the Terrestrial Ecosystem Model (TEM) (Raich et al. 1991).

$$T_{scaler} = \frac{(T - T_{max}) \times (T - T_{min})}{(T - T_{max}) \times (T - T_{min}) - (T - T_{opt})^2} \qquad (10)$$

where T_{min}, T_{max} and T_{opt} are the minimum, maximum, and optimum temperatures for vegetation photosynthesis, respectively. These parameters are biome specific and are also obtained from the LUT. The limitation from water stress is estimated from LSWI:

$$W_{scalar} = \frac{1 + LSWI}{1 + LSWI_{max}} \qquad (11)$$

259    $LSWI_{max}$ is the maximum LSWI during the growing season over several years. We

260   delineate the $LSWI_{max}$ for plant growing season from the following steps: (1) during the

261   growing season period pre-defined by the LST, $LSWI_{max}$ is retrieved as the yearly maximum

262   LSWI. If temperature-based identification of the growing season fails in the boreal region

263   where nighttime temperature is always below 10℃, the growing season is set to be June to

264   August. (2) LSWI will have an abnormally high value if snow exists and a lower value during

265   drought periods. To eliminate these abnormal values and take the land cover change into

266   consideration, we further calculate the $LSWI_{max}$ using a moving-window statistical algorithm:

267   we select a window of five years and pick the second largest maximum LSWI in this period.

268
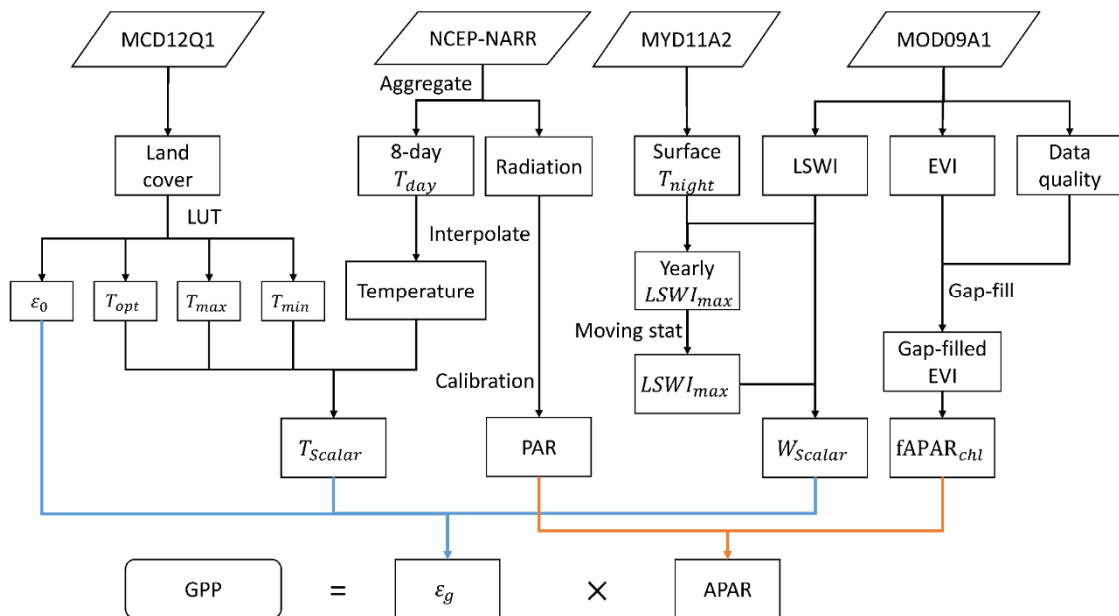
269
270   Fig. 2. Flowchart of the data processing procedures for vegetation photosynthesis model
271   (VPM).

272

3. Results

3.1. Seasonal dynamics of GPP at individual flux tower sites

Fig. 3 shows the seasonal dynamics and interannual variations of GPP_{EC} and GPP_{VPM} across the 39 flux tower sites. The VPM accurately predicts the seasonality and magnitude of GPP for most natural vegetation (vegetation types other than cropland and cropland/natural vegetation mosaic in IGBP classification) (Fig. 3). Table 1 summarizes the correlation between GPP_{EC} and GPP_{VPM} at individual sites over years. Nearly two thirds of the natural biomes sites have a RMSE < 1.5 g C m^{-2} day^{-1}. Cropland sites have slightly larger RMSE values of 2.20 – 3.06 g C m^{-2} day^{-1}

Table 1. Descriptions of the 39 flux tower sites used in this study. IGBP class, R^2, and RMSE are the International Geosphere-Biosphere Programme land cover classification, coefficient of determination, and root mean square error of the regression analysis between tower-based gross primary production (GPP_{EC}) and simulated GPP (GPP_{VPM}) using vegetation photosynthesis model.

ID	NAME	LAT	LON	IGBP class	Years used	R^2	RMSE	Reference
US-Bo1	Bondville	40.0062	-88.2904	CRO	2001-2006	0.83	2.20	Hollinger et al. (2005)
US-Ne1	Mead irrigated continuous	41.1651	-96.4766	CRO	2001-2005	0.91	3.06	Suyker et al. (2005)
US-Ne2	Mead irrigated rotation	41.1649	-96.4701	CRO	2001-2005	0.91	2.71	Suyker et al. (2005)
US-Ne3	Mead rainfed rotation	41.1797	-96.4397	CRO	2001-2005	0.85	2.76	Suyker et al. (2005)
US-Ro1	Rosemount-G21	44.7143	-93.0898	CRO	2004-2006	0.80	2.45	Griffis et al. (2005)
US-Ro3	Rosemount-G19	44.7217	-93.0893	CRO	2004-2006	0.81	2.22	Griffis et al. (2005)

US-KS2	Kennedy Space Center	28.6086	-80.6715	CSH	2004-2005	0.72	0.96	Dijkstra et al. (2002)
US-Los	Lost Creek	46.0827	-89.9792	CSH	2001-2002	0.90	1.59	Sulman et al. (2009)
US-Bar	Bartlett Experimental Forest	44.0646	-71.2881	DBF	2004-2006	0.93	1.33	Jenkins et al. (2007)
US-Ha1	Harvard Forest	42.5378	-72.1715	DBF	2000-2006	0.83	2.05	Urbanski et al. (2007)
US-LPH	Little Prospect Hill	42.5419	-72.1850	DBF	2001-2005	0.91	1.30	Vanderhoof et al. (2013)
US-MMS	Morgan Monroe State Forest	39.3232	-86.4131	DBF	2005-2007	0.91	1.59	Schmid et al. (2000)
US-MOz	Missouri Ozark Site	38.7441	-92.2000	DBF	2000-2006	0.89	1.37	Gu et al. (2006)
US-UMB	Univ. of Mich. Biological Station	45.5598	-84.7138	DBF	2000-2006	0.97	0.78	Gough et al. (2008)
US-WCr	Willow Creek	45.8059	-90.0799	DBF	2002-2005	0.96	1.05	Cook et al. (2004)
CA-NS1	UCI-1850 burn site	55.8792	-98.4839	ENF	2003-2005	0.65	1.00	Goulden et al. (2006)
CA-NS2	UCI-1930 burn site	55.9058	-98.5247	ENF	2002-2005	0.70	0.88	Goulden et al. (2006)
CA-NS3	UCI-1964 burn site	55.9117	-98.3822	ENF	2002-2005	0.92	1.49	Goulden et al. (2006)
CA-NS4	UCI-1964 burn site wet	55.9117	-98.3822	ENF	2003-2004	0.84	1.08	Goulden et al. (2006)
CA-NS5	UCI-1981 burn site	55.8631	-98.4850	ENF	2002-2005	0.89	1.13	Goulden et al. (2006)
US-Blo	Blodgett Forest	38.8953	-120.6328	ENF	2000-2006	0.74	1.58	Goldstein et al. (2000)
US-Fmf	Flagstaff Managed Forest	35.1426	-111.7273	ENF	2007	0.63	0.95	Dore et al. (2008)
US-Ho1	Howland Forest (main tower)	45.2041	-68.7402	ENF	2000-2004	0.88	0.84	Hollinger et al. (2004)
US-Ho2	Howland Forest (west tower)	45.2091	-68.7470	ENF	2000-2004	0.69	0.98	Hollinger et al. (2004)

|								
US-Me2	Metolius-intermediate aged pine	44.4523	-121.5574	ENF	2002, 2004-2007	0.91	1.03	Law et al. (2004)
US-Me3	Metolius-second young aged pine	44.3154	-121.6078	ENF	2004-2005	0.69	1.26	Law et al. (2000)
US-Me5	Metolius-first young aged pine	44.4372	-121.5668	ENF	2000-2002	0.94	0.60	Law et al. (2000)
US-NC1	North Carolina Clearcut	35.8115	-76.7115	ENF	2005-2006	0.95	0.93	Noormets et al. (2010)
US-Wi0	Wisconsin young red pine	46.6188	-91.0814	ENF	2002	0.81	1.79	Sun et al. (2008)
US-Wi4	Wisconsin mature red pine	46.7393	-91.1663	ENF	2002-2005	0.92	0.81	Sun et al. (2008)
US-ARb	ARM SGP burn	35.5497	-98.0402	GRA	2005-2006	0.91	1.99	Fischer et al. (2007)
US-ARc	ARM SGP control	35.5465	-98.0400	GRA	2005-2006	0.91	2.07	Fischer et al. (2007)
US-Goo	Goodwin Creek	34.2547	-89.8735	GRA	2004-2006	0.68	1.93	Wilson and Meyers (2007)
US-Wlr	Walnut River Watershed	37.5208	-96.8550	GRA	2002-2004	0.94	0.81	Coulter et al. (2006)
US-Syv	Sylvania Wilderness Area	46.2420	-89.3477	MF	2001-2006	0.92	1.12	Desai et al. (2005)
CA-NS6	UCI-1989 burn site	55.9167	-98.9644	OSH	2002-2005	0.87	0.69	Goulden et al. (2006)
CA-NS7	UCI-1998 burn site	56.6358	-99.9483	OSH	2002-2005	0.86	0.63	Goulden et al. (2006)
US-Ivo	Ivotuk	68.4865	-155.7503	WET	2004, 2006	0.67	0.80	Epstein et al. (2004)
US-FR2	Freeman Ranch-Mesquite Juniper	29.9495	-97.9962	WSA	2004-2006	0.73	1.13	Heinsch et al. (2004)

288   CRO: cropland; CSH: closed shrublands; DBF: deciduous broadleaf forests; ENF:
289 evergreen needleleaf forest; GRA: grassland; MF: mixed forest; OSH: open shrublands; WET:
290 wetland; WSA: woody savannas.

291

292   Fig. 4 shows the comparison between GPP_{EC} and GPP_{VPM} at biome levels. When

293   compared to GPP_{EC}, GPP_{VPM} underestimate by 4% (according to regression slope and hereafter)

294   for deciduous broadleaf forests (DBF), 8% for mixed forests (MF), and 16% for evergreen

295   needleleaf forests (ENF). GPP_{VPM} and GPP_{EC} agree well for closed shrubland (2%) and open

296   shrubland (4%). For grassland and woody savannas (WSA), the biases are < 8%. When all

297   natural biome sites are combined, GPP_{VPM} is slightly lower than GPP_{EC}, approximately 8% (y

298   = 0.92x, R^2 = 0.85) (Fig. 4). For cropland sites (cropland and cropland/natural vegetation

299   mosaic in IGBP classification), GPP_{VPM} is lower than GPP_{EC} by 23% (y = 0.77x, R^2 = 0.82).

300   When all 39 sites are lumped together, the difference between GPP_{VPM} and GPP_{EC} is

301   approximately 13% (y = 0.87x, R^2 = 0.82). The LUE parameter in VPM improves the

302   predictability of GPP, as represented by the decreased coefficient of determination (R^2) in the

303   VPM model sensitivity analysis for both natural biomes and all biomes sites when LUE

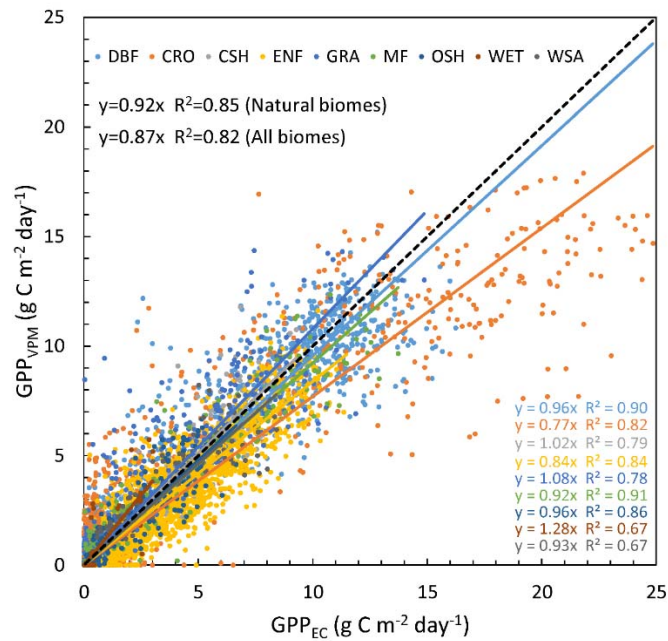304   parameter is removed (Fig. A1).

305
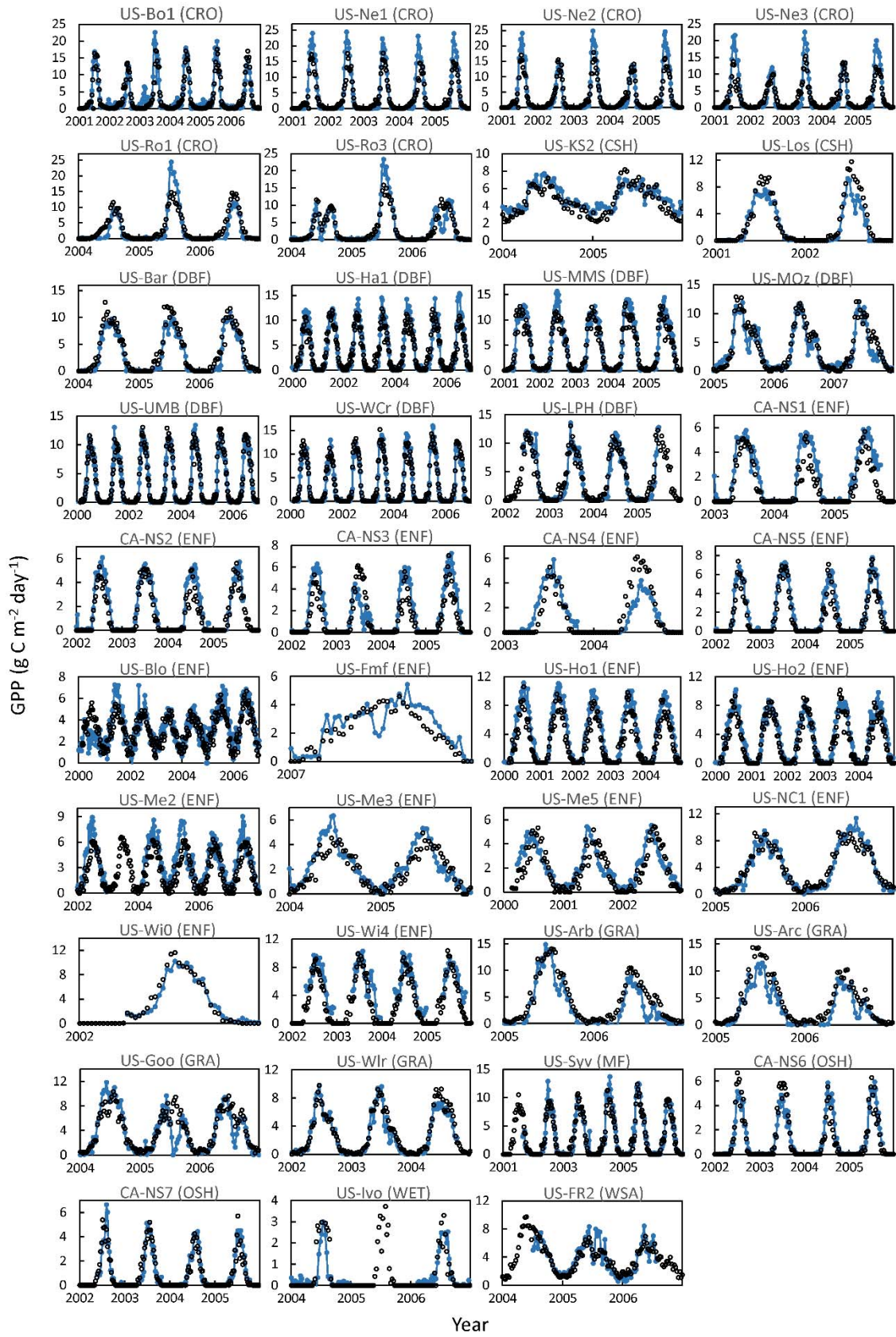
306
307　Fig. 3. Seasonal dynamics and interannual variations of the tower-based (GPP$_{EC}$) and the
308　modeled (GPP$_{VPM}$) gross primary production at 39 flux sites at 8-day intervals. The blue lines

represent the GPP_{EC} and the black circles represent the GPP_{VPM}. The ticks on the x-axis represent the first date of the corresponding year.


Fig. 4. A comparison of the tower-based (GPP_{EC}) and the modeled (GPP_{VPM}) gross primary production by biome types. Data are pooled across the study period for each biome. The dash line is 1:1 line and solid lines are linear regression lines forced to pass the origin.

3.2. Spatial patterns of GPP_{VPM} across North America in 2010 at 500-m spatial resolution

Fig. 5A shows the spatial distribution of annual GPP_{VPM} for 2010 across NA. The highest GPP_{VPM} (> 2,000 g C m^{-2} year^{-1}) occurs in the southernmost tropical regions. GPP_{VPM} decreases along a latitudinal gradient in the eastern region, owing to the decreasing temperature and growing season length. GPP_{VPM} also decreases along a longitudinal gradient from east (dominated by forest) to west (dominated by grasslands and desert). Fig. 5B shows the spatial distribution of the maximum daily GPP_{VPM} in 2010. The highest value is ~20 g C m^{-2} day^{-1} for the Midwest Corn Belt. The southeastern U.S. has a relatively low value as compared with the

mid-latitude region (35°N - 45°N). The biggest contrast between annual GPP$_{VPM}$ and maximum

daily GPP$_{VPM}$ is found in the tropical and western coastal regions, where annual GPP$_{VPM}$ is

highest while the maximum daily GPP$_{VPM}$ is moderate.
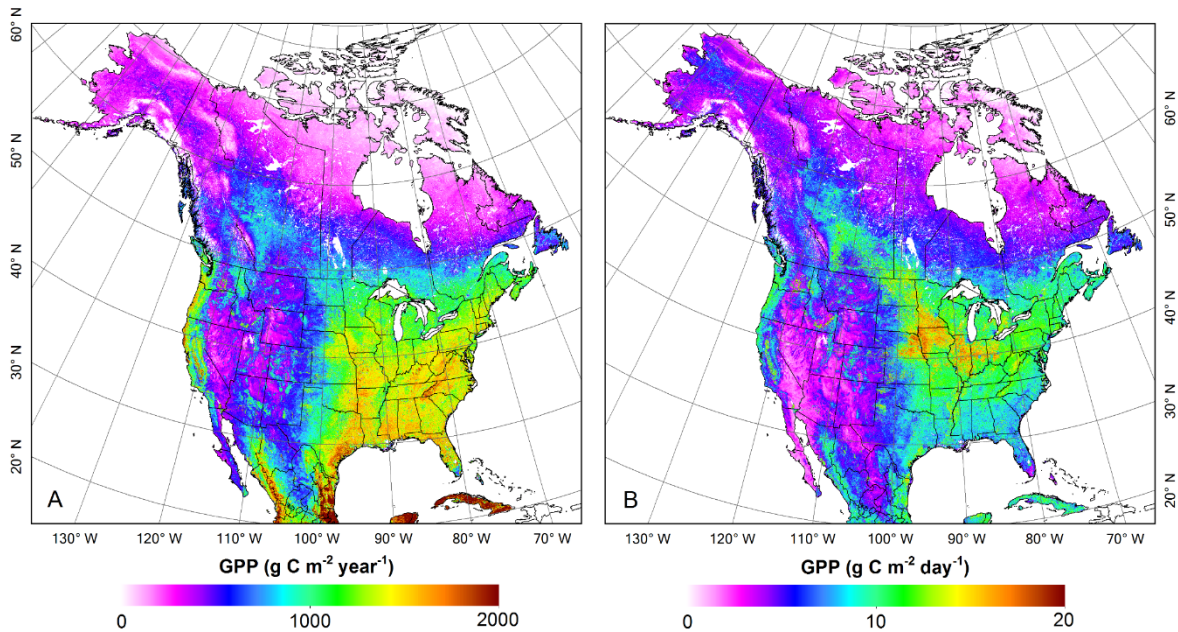
Fig. 5. Spatial distribution of modeled (A) annual GPP$_{VPM}$ and (B) maximum daily GPP$_{VPM}$
for year 2010.

GPP$_{VPM}$ varies significantly across biomes (Table 2). The most productive ecosystem is the

evergreen broadleaf forest with an annual GPP$_{VPM}$ of > 2,000 g C m^{-2} year^{-1}. Open shrubland

and savannas are the least productive with an annual GPP$_{VPM}$ < 375 g C m^{-2} year^{-1}. Grassland,

savannas, and shrublands have relatively high spatial variance because of the extensive

distribution and high sensitivity to soil water. All natural vegetation contribute about 70% of

the total GPP$_{VPM}$, with an average of 600.88 g C m^{-2} year^{-1}. Croplands accounts for about 27%

of the total GPP but with a nearly doubled photosynthetic capacity (1,194.27 g C m^{-2} year^{-1})

compared with the mean of natural vegetation. The maximum daily GPP$_{VPM}$ for different

341　biomes varies from 3.59 to 12.00 g C m^{-2} day^{-1}. Croplands have the largest GPP$_{VPM}$ magnitudes

342　(9.94 to 12.00 g C m^{-2} day^{-1}). Forest ecosystems have a relatively higher maximum

343　photosynthetic rate (8.79 g C m^{-2} day^{-1}) compared with other natural vegetation types (4.65 g

344　C m^{-2} day^{-1}). The inconsistency between annual GPP$_{VPM}$ sums and maximum daily GPP$_{VPM}$

345　may be mainly attributed to different growing season lengths that are affected by temperatures

346　and rainfall.

347

348　Table 2. The magnitudes and annual sums of simulated gross primary production (GPP$_{VPM}$)
349　of different biomes in North America (170°~50°W, 20°~80°N) for year 2010.

| IGBP class	Average annual GPP (g C m^{-2} year^{-1})	Standard deviation of annual GPP (g C m^{-2} year^{-1})	Average maximum daily GPP (g C m^{-2} day^{-1})	Standard deviation of maximum daily GPP (g C m^{-2} day^{-1})	Total (Pg C year^{-1})
ENF	638.45	255.53	5.90	1.55	1.32
EBF	2038.76	448.32	9.63	1.71	0.16
DBF	1443.95	188.49	11.09	1.47	0.75
MF	1030.24	330.46	8.53	1.78	1.94
OSH	349.30	224.44	3.59	1.31	1.48
WSA	815.81	543.79	6.27	2.29	1.50
SAV	377.65	267.02	4.17	1.27	0.20
GRA	457.50	380.74	4.24	2.59	2.00
WET	539.26	253.98	5.00	1.41	0.21
CRO	1157.99	390.54	12.00	3.09	2.15
CNV	1248.95	317.55	9.94	1.67	1.54

350　　ENF: evergreen needleleaf forest; EBF: evergreen broadleaf forest; DBF: deciduous
351　broadleaf forest; MF: mixed forest; OSH: open shrubland; WSA: woody savannas; SAV:
352　savannas; GRA: grassland; WET: wetland; CRO: cropland; CNV: cropland/natural vegetation
353　mosaic.

354

355　　Fig. 6 shows the frequency distribution of annual GPP$_{VPM}$ and maximum daily GPP$_{VPM}$ for

356　all pixels in NA and their distribution in the climate space. More than 70% of pixels have

357　relatively low productivity, i.e., annual GPP$_{VPM}$ less than 1,000 g C m^{-2} year^{-1} or maximum

358 daily GPP$_{VPM}$ less than 10 g C m^{-2} day^{-1}. We also plot the distribution of the 39 flux tower sites

359 in NA based on the annual and maximum daily GPP$_{EC}$ (Fig. 6). The distribution of the flux

360 tower sites cover the broad range of maximum daily GPP$_{VPM}$, and most of them are located in

361 regions with moderate annual GPP (1,000 – 1,800 g C m^{-2} year^{-1}). In the two-dimensional

362 climate space described by mean annual temperature (MAT) and mean annual precipitation

363 (MAP) (Fig. 6C, D), the flux tower sites distribution covers most of the climate space. The

364 annual GPP$_{VPM}$ generally increases with MAT mad MAP, while the daily maximum GPP$_{VPM}$ is

365 highest in moderate MAT and MAP regions.

366

367
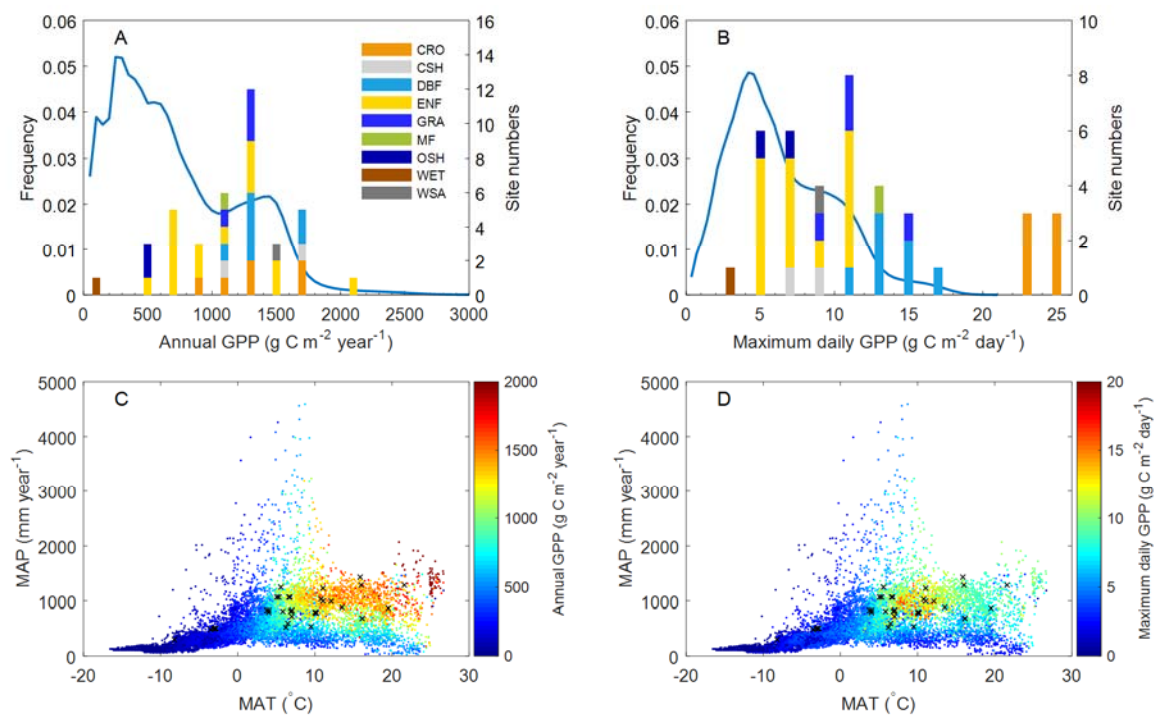
368
369 Fig. 6. The frequency distribution of GPP$_{VPM}$ of the (A) annual GPP and (B) maximum daily
370 GPP compared to the flux site distribution and their distribution in the climate space defined
371 by mean annual temperature (MAT) mean annual precipitation (MAP) (C, D). The blue curves
372 in (A and B) indicate the frequency distribution calculated from Fig. 5. The annual and
373 maximum daily GPP for the flux tower sites are from the 39 sites used in our study. Black
374 crosses in (C and D) represent the location of 39 flux tower sites in the climate space.

375 Precipitation data from GPCC (Global Precipitation Climatology Centre) and temperature data

376 from NCEP-NARR are used to generate the climate space.

377

378 3.3. Spatial-temporal comparison between GPP$_{VPM}$ and SIF across NA in 2010 at 0.5

379 degree spatial resolution

380   We aggregate the 8-day 500-m GPP$_{VPM}$ estimates to the seasonal (3-month interval) and

381 0.5° latitude/longitude grid to compare with the seasonal SIF data. Both GPP$_{VPM}$ and GOME-

382 2 SIF data have strong seasonal dynamics and spatial variation across NA (Fig. 7, 8).

383   During spring (March to May), both GPP$_{VPM}$ and GOME-2 SIF are relatively high in the

384 southeastern part of the United States (Fig. 7), where forests dominate and plants grow through

385 the spring. Both GPP$_{VPM}$ and GOME-2 SIF are also high in California, where the

386 Mediterranean climate (warm and wet spring and dry summer) is located (Ma et al. 2007; Xu

387 and Baldocchi 2004). In comparison, the rest of lands with low temperature and/or rainfall in

388 NA have low GPP$_{VPM}$ and GOME-2 SIF values.

389
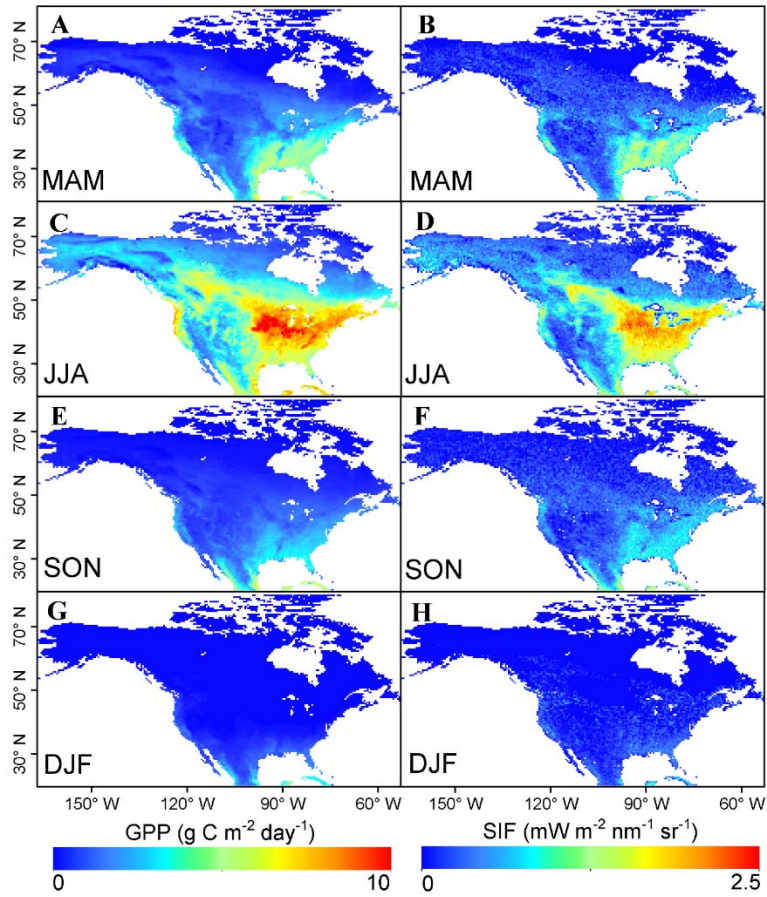
Fig. 7. A comparison of seasonal average solar-induced fluorescence (SIF) from the GOME-2 satellite instrument and simulated gross primary production (GPP$_{VPM}$) during the period of March 2010 through February 2011. MAM, JJA, SON, and DJF correspond to spring, summer, fall, and winter, respectively.

In summer months (June to August), the Corn Belt in mid-west U.S. and southwestern Canada has the highest GPP$_{VPM}$ and SIF. This is supported by the eddy flux data: GPP$_{EC}$ for maize is > 25 g C m^{-2} day^{-1} during summer, much higher than that of the forest ecosystems. Overall, summer months contribute > 62% of the annual GPP in NA, 42% of which come from Canada and 45% from the conterminous U.S. SIF data also show the highest values in the Corn Belt and lowest in the western and northern regions, consistent with the GPP$_{VPM}$.

In the fall (September to November), both GPP$_{VPM}$ and SIF drop substantially in the mid-

403 west region due to crop harvesting. Similar to spring, the high photosynthesis rate also

404 corresponds to a long growing season in the southeastern U.S., but the value is smaller than

405 spring. The eastern and western coasts of Mexico as well as Cuba still fix carbon at a rate of

406 more than 5 g C m^{-2} day^{-1}. In Alaska and northern Canada, all vegetation goes to dormancy,

407 and both GPP$_{VPM}$ and SIF values are close to 0. These spatial patterns are also evident in the

408 SIF data.

409   During the winter (December through February), only the very southern part of the U.S.,

410 California, and coastal regions of Mexico and Cuba have moderate GPP$_{VPM}$ and SIF values.

411 All the other regions do not show any sign of photosynthesis activities, and both GPP$_{VPM}$ and

412 SIF values are close to zero.

413 **4. Discussion**

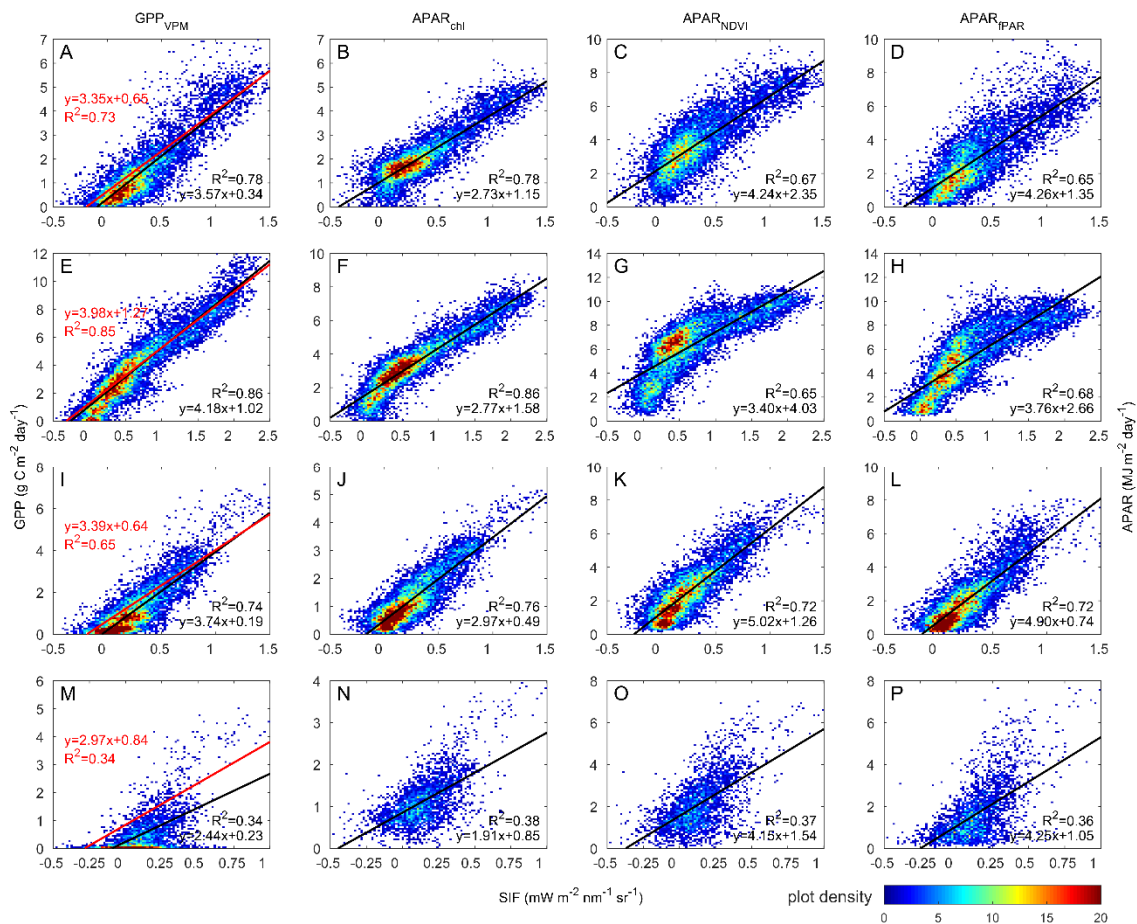414 **4.1.The relationship between SIF and GPP**

415   SIF is emitted during the vegetation photosynthetic process. Absorbed energy by

416 chlorophyll is partitioned into SIF, photochemical quenching (PQ, energy used for

417 photosynthesis), non-photochemical quenching (NPQ, energy partitioned to heating), and

418 efficiency loss (Baker 2008). Previous studies have shown that SIF is positively correlated with

419 PQ when light is moderate or high or environmental stress exists (Flexas et al. 2000; Lee et al.

420 2015; Porcar-Castell et al. 2006; Soukupová et al. 2008). However, the relationship between

421 GPP and SIF emission at far-red peak (SIF$_{740}$ used in our study) is also affected by the SIF

422 contribution from photosystem II and photosystem I, alternative sinks of energy,

423 photorespiration, internal CO_2 concentration of leaves and enzyme activities, etc. (Porcar-

424 Castell et al. 2014). Although SIF measurements from satellite provide a direct and independent

425 estimations of photosynthetic activity which is different from reflectance based vegetation

426 indices, the GPP-SIF relationship still needs intensive investigation.

427 Several studies (Joiner et al. 2014; Zhang et al. 2014; Wagle et al. 2016) have reported on

428 the direct comparison between satellite-derived SIF data (0.5° grid cell) and *in situ* GPP_{EC} from

429 flux sites that often have footprint sizes of a few hundreds of meters, but such comparisons is

430 problematic owing to spatial mismatches and heterogeneity due to mixed land cover types

431 within a given 0.5° grid cell (Zhang et al. 2014). In this study, the VPM simulations are

432 aggregated to the same spatial resolution as the GOME-2 SIF data. Fig. 8 shows the correlation

433 between GPP_{VPM} and the SIF data for the four seasons. In spring, summer, and fall, GPP_{VPM}

434 shows a very high correlation with SIF. The coefficient of determination ranges from 0.74 to

435 0.86, and the GPP_{VPM}-SIF correlation increases with the increase in daily GPP or SIF value

436 (from early to peak growing season). This high spatial correlation confirms our comparison in

437 section 3.3 and can be further explained by the $APAR_{chl}$ used in the VPM. Both $APAR_{NDVI}$

438 (NDVI*PAR) and $APAR_{fPAR}$ (fPAR*PAR) have lower correlation with SIF compared with

439 $APAR_{chl}$; an obvious saturation can be found in summer where SIF continues to increase while

440 $APAR_{NDVI}$ and $APAR_{fPAR}$ tend to saturate. The regression slope between $APAR_{chl}$ and SIF are

441 also more stable during the growing season (2.82 ± 0.13). As SIF is reemitted from the

442 photosystem II, the higher correlation between SIF and $APAR_{chl}$ also suggests that EVI can be

443 a good proxy of light absorbed by chlorophyll. In the winter, however, the correlations between

444   SIF and GPP$_{VPM}$ and APAR are much weaker mostly due to the very low SIF signal and

445   relatively lower signal-to-noise ratio. We also calculate the regression between GPP$_{VPM}$ and

446   SIF for points with GPP$_{VPM}$ > 1 g C m^{-2} day^{-1} (to eliminate some low values with relatively

447   higher bias during the non-growing season). The range of the regression slopes are narrower

448   when only data for the period of GPP$_{VPM}$ > 1g C m^{-2} day^{-1} are used as compared to all data

449   points (SD$_{slope}$=0.42 vs. 0.74).

450

451

452   Fig. 8. Relationship between SIF and GPP$_{VPM}$ (A, E, I, M), APAR$_{chl}$ (EVI*PAR) (B, F, J, N),
453   APAR$_{NDVI}$ (NDVI*PAR) (C, G, K, O) and APAR$_{fPAR}$ (fPAR*PAR) (D, H, L, P) for four seasons
454   (by row from first to fourth: spring, summer, autumn, winter) in North America in 2010. EVI
455   and NDVI are from monthly 0.05° MOD13C1 C5, fPAR is from 8-day 1km MOD15A2 C5,
456   all of which are aggregated to seasonal and 0.5-degree spatial resolution. Black lines are
457   regression for all the points, and the red lines are the regressions between GPP$_{VPM}$ and SIF with

458 $GPP_{VPM} > 1$ g C m^{-2} day^{-1}.

459

460   4.2. Comparison of SIF and GPP estimates in North America from several models

461   A number of models have reported annual total GPP in NA (Huntzinger et al. 2012; Xiao

462   et al. 2014). The annual GPP_{VPM} is 13.53 Pg C in 2010. We further compared GPP_{VPM} with

463   GPP from six other models (MODIS PSN, MPI-BGC, LPJ, LPJ-GUESS, ORCHIDEE, and

464   VEGAS) (Fig. 9). The VPM-based GPP estimates are close to the average of these six models

465   (15.75 Pg C year^{-1}) (Table 3). Three process-based models (LPJ, LPJ-GUESS, and ORCHIDEE)

466   predict very high GPP for the southeastern U.S., which may be caused by different approaches

467   they employed (enzyme kinetic vs. LUE).

468   Because SIF is directly retrieved from satellite and has a very good correlation with data

469   driven model-based GPP (Frankenberg et al. 2011; Wagle et al. 2016), we use SIF as a reference

470   to compare the spatial variations in GPP of all models. ORCHIDEE, PSN, MPI-BGC, and

471   VPM show high consistency with SIF data. The major difference is the relative underestimation

472   at the Corn-Belt and overestimation in the western coast along the U.S./Canada border in

473   ORCHIDEE, PSN, and MPI-BGC. Recent studies reveal that cropland, especially maize in the

474   U.S., makes a large contribution to the seasonal swing of atmospheric CO_2 concentration (Gray

475   et al. 2014; Zeng et al. 2014). The high GPP values in this region are often underestimated by

476   models (Guanter et al. 2014). Beer et al. (2010) also suggest that given the limited C4

477   vegetation flux data availability, great uncertainty remains in estimating the contribution of C4

478   plants while upscaling eddy flux observations. A similar issue is also found in a study focused

479 on the conterminous U.S. (Xiao et al. 2010), which may explain the underestimation of the

480 regional GPP sums. GPP$_{VPM}$ and SIF data show similar spatial patterns for the mid-western

481 Corn Belt (r = 0.87, p < 0.001) where a previous study showed SIF at a monthly scale has a

482 high correlation with GPP (Guanter et al. 2014); this also supports that the spatial variation of

483 GPP$_{VPM}$ for croplands is to some degree an improvement over the other six models.

484
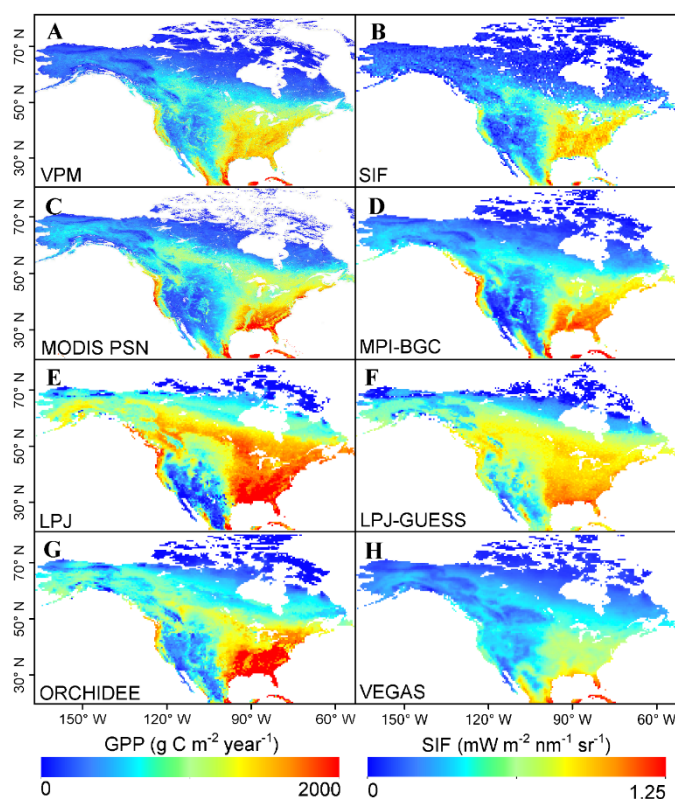
485
486 Fig. 9. Comparison of annual gross primary production (GPP) from different LUE-based
487 models (A, C), data-driven model (D), process-based models (E, F, G, H), and with solar-
488 induced fluorescence (SIF) (B). Data are shown for the year 2010.

489

490 Table 3. Annual gross primary production (GPP) of North America (170°~50°W, 20°~80°N)
491 estimated from different models for year 2010.

Models	Annual GPP (Pg C year^{-1})	Reference
LPJ	22.23	Sitch et al. (2003)
LPJ-GUESS	19.84	Smith et al. (2001)
ORCHIDEE	17.52	Krinner et al. (2005)

VEGAS	11.35	Zeng et al. (2005)
MODIS GPP	13.13	Zhao et al. (2005)
MPI-BGC	12.70	Jung et al. (2011)
VPM	13.53	This study

492

493   Several previous studies indicate that the relationships between GPP and SIF should be

494   different across biomes (Damm et al. 2015; Guanter et al. 2012; Guanter et al. 2014; Parazoo

495   et al. 2014; Verrelst et al. 2015). This ecosystem-dependent GPP-SIF relationship is determined

496   by different SIF contribution from both photosystem I and photosystem II, uncertainty in NPQ,

497   and structural interference of SIF leaving the canopy (Damm et al. 2015; Verrelst et al. 2015).

498   Here we compare SIF with GPP estimates from three diagnostic models (VPM, MPI-BGC, and

499   MODIS PSN) and $APAR_{chl}$, as well as the relationship between SIF_{yield} ($SIF/APAR_{chl}$) and LUE

500   (Fig. 10). Being consistent with a previous study at site level (Yang et al. 2015), we also find

501   that SIF contains the information of LUE, represented by a high correlation between SIF_{yield}

502   ($SIF/APAR_{chl}$) and LUE_{VPM} (Fig. 10E). This also partially supports the GPP-SIF relationship.

503   However, due to the spatial inconsistency, we did not directly compare GOME-2 SIF_{yield} with

504   LUE_{EC}, more canopy or ecosystem level SIF measurement from *in situ* or airborne

505   spectrometers will enable this kind of comparison in the near future. In terms of inter-model

506   comparison, VPM and MPI-BGC show higher average R^2 (0.86 and 0.89, respectively) for

507   individual biomes than does MODIS PSN (0.83). The data points are also more scattered in the

508   MODIS PSN than in other two models. Different biome types also show distinct differences in

509   slopes (4.03 – 8.9 for VPM, 3.73 – 7.83 for MPI-BGC, and 2.76 – 11.12 for MODIS PSN). For

510   the most highly productive biomes (average SIF > 1 mW m^{-2} nm^{-1} sr^{-1}), the correlations

511   between predicted GPP and SIF are very high ($R^2 > 0.95$) except for EBF; this may be caused

512   by cloud and/or aerosol contamination of the satellite data. The range of slopes for these biomes

513   also shows less variation (4.60 – 5.55 for VPM, 4.02 – 5.72 for MPI-BGC, and 3.60 – 6.02 for

514   MODIS PSN). In contrast, the less productive regions usually have lower regression

515   coefficients and more variable slopes. This may be partially due to the higher relative error for

516   the GOME-2 SIF data (Joiner et al. 2013) and GPP models. SIF retrievals from later satellites

517   (OCO-2, FLEX - Fluorescence Explorer, Sentinel-5 Precursor) will have better accuracy

518   (Frankenberg et al. 2014; Guanter et al. 2015; Kraft et al. 2013) and can be used to improve

519   and benchmark GPP for land models (Lee et al. 2015; Luo et al. 2011; Zhang et al. 2014).

520
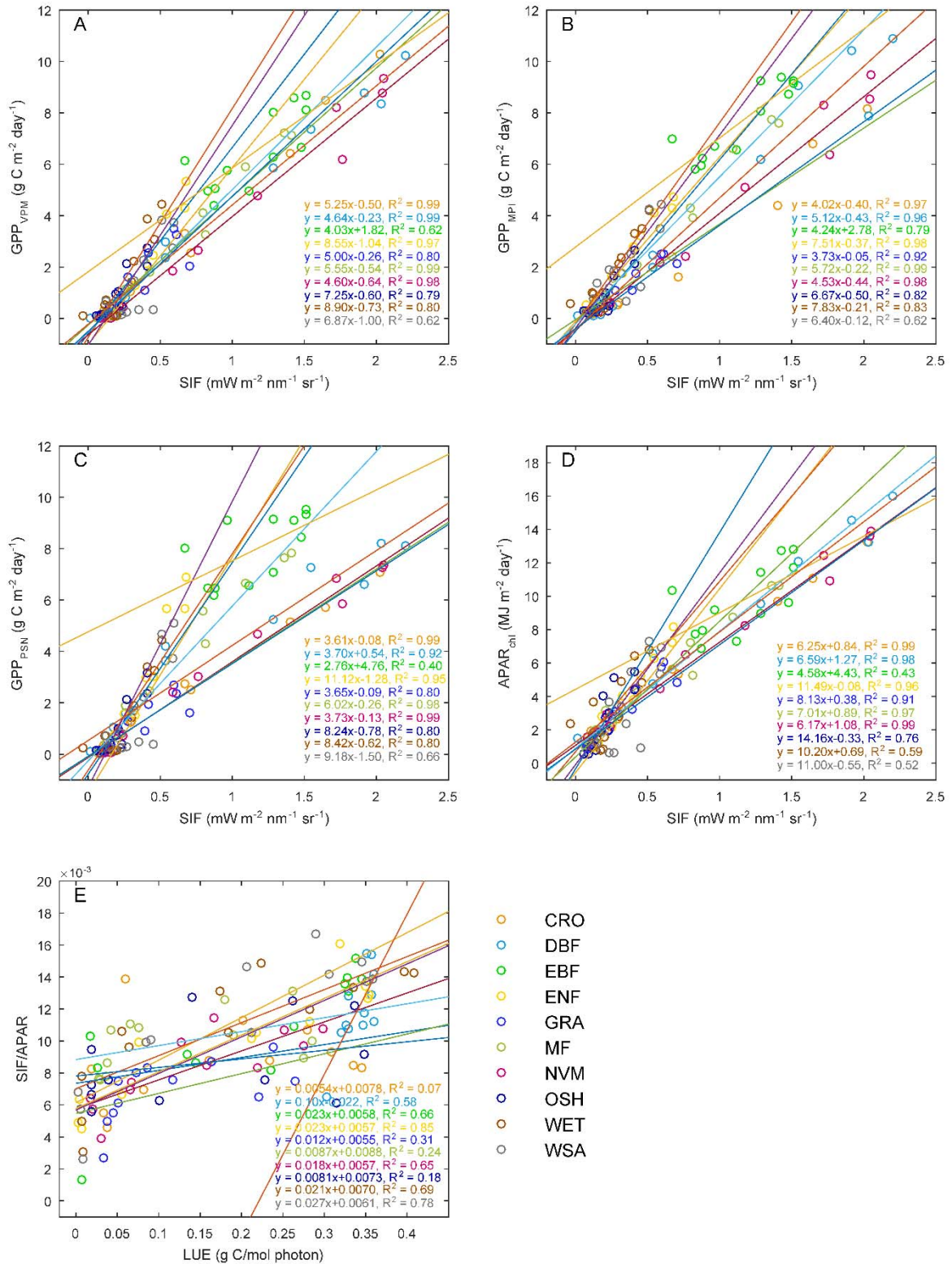
521
522 Fig. 10. A comparison for relationship between GPP$_{VPM}$ and SIF (A), GPP$_{MPI}$ and SIF (B),
523 GPP$_{PSN}$ and SIF (C), APAR$_{chl}$ (EVI*PAR) and SIF (D), SIF$_{yield}$ (SIF/APAR) and LUE$_{VPM}$ (E)
524 for different biome types in North America in 2010. For each month each biome type, a value
525 is given by spatially averaging all the grid cells with in this biome type.
526

4.3. Sources of uncertainty for VPM simulations in North America

527

Maps of land cover types affect GPP estimates as the LUE parameter used in the model varies with biomes. In this study, the MOD12 land cover dataset lists croplands as one category and does not distinguish between C3 and C4 crops. Both C3 and C4 crops have different photosynthetic pathways and light use efficiency (Kalfas et al. 2011; Yuan et al. 2015): C4 crops (e.g., maize) have a higher GPP_{EC} than do C3 crops (Fig. 3). Thus, the LUE parameterization of croplands for each year depends upon our knowledge of crop types and rotation. For VPM simulations at the continental scale, there are four options to address this problem in a MODIS cropland pixel: (1) assume 100% C3 plants, (2) assume 100% C4 plants, (3) assume C3+C4 mixing ratio as 50% each, and (4) use known C3+C4 mixing ratio from other data sources (*in situ* data, or other maps). Because there is no yearly map of C3/C4 mixing ratio across NA, we simply chose the third option in this study. Therefore, GPP_{VPM} would either overestimate GPP for C3 plants (soybean, wheat, etc.) or underestimate for C4 plants (corn, sugar cane, etc.) in those pure pixels. In those C3/C4 mixed pixels, however, these artifacts (under- or over-estimation) can be partially alleviated. For example, both maize and soybean are grown in rotation at the US-Bo1 site within a 50 m radius, but within a 500 m radius of the flux tower site, corn and soybean areas have a mixing ratio of 50% each over the years. The GPP_{VPM}, driven by averaged LUE for C3 and C4 crops, captures both the seasonality and the magnitude at this site (Fig. 11A). For pure pixels, VPM would provide better results if a specific crop type is given and an appropriate LUE value is used. We use the LUE value for C4 plants at the US-Ne1 site where maize is grown throughout the period (Fig. 11B). This modification

548　greatly improves the estimation of GPP, with an RMSE reduces from 3.06 to 2.32 g C m^{-2} day^{-}

549　^{1} and the slope increases from 0.65 to 0.86.

550
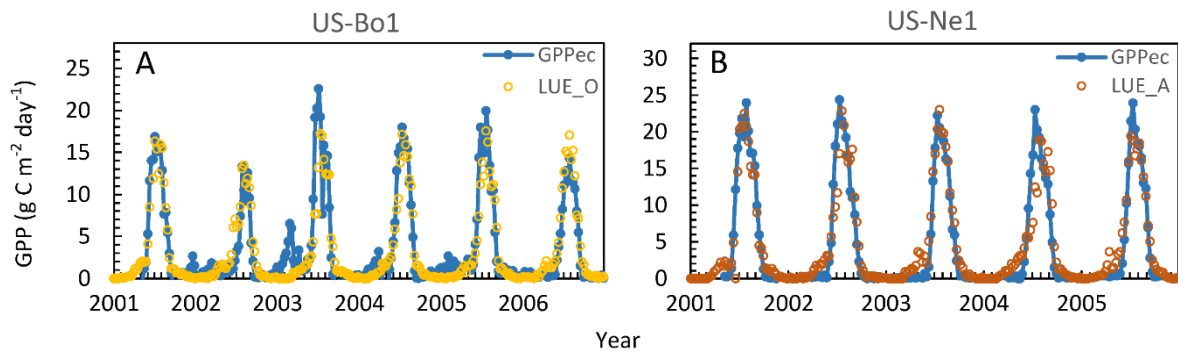
551

552　Fig. 11. Seasonal dynamics and interannual variations of the tower-based (GPP$_{EC}$) and the
553　modeled (GPP$_{VPM}$) gross primary production at two flux tower sites at 8-day intervals at a
554　maize/soybean rotation site (US-Bo1) (A) and a continuous maize site (US-Ne1) (B). Blue
555　lines represent estimated GPP from flux tower, yellow circles represent the present simulation
556　result using the original LUE (LUE_O) and brown circles represent improved simulation result
557　using an alternative LUE (LUE_A) for C4 plant.

558

559　　　In our study, all cropland flux tower sites are located in the mid-west Corn Belt and

560　altogether we have 16 corn years and 11 soybean years. As we use an average LUE of C3 and

561　C4 for croplands, the model may underestimate GPP at the site scale owing to more corn years

562　(Fig. 4.). At a regional scale, the bias mainly depends on the C3 and C4 crop mixing ratios

563　within individual pixels. In the U.S. Midwest where C4 crops (e.g., maize) are dominant, the

564　VPM simulation may underestimate cropland production while in California or the Mississippi

565　River Basin, where C3 crops are dominant, the VPM simulation may overestimate. Therefore,

566　the lack of crop plant functional type (C3 and C4) is likely the largest source of uncertainty in

567　the GPP$_{VPM}$. This clearly highlights the need to generate annual maps of plant functional types

568　(C3 and C4) in NA in the near future. In addition, the mismatch between the flux tower footprint

569　and the MODIS pixel, and the land cover fragmentation within each MODIS pixel are also

570　critical issues when using EC data for model validation. All flux towers should be evaluated

571　using footprint models and high resolution satellite images to provide the representativeness

572　for the MODIS pixel (Chen et al. 2012).

573　　Image data quality is always an important issue for the application of remote sensing. In

574　this study, we use the vegetation indices calculated directly from the MODIS surface

575　reflectance product. These indices are subject to atmospheric contamination (i.e., clouds,

576　aerosols) and often result in a lower-than-normal value for EVI, especially in those regions

577　where cloud and aerosol are persistent (boreal and tropical regions in our study). The effect of

578　the atmospheric contamination can be partially eliminated through a gap-fill method. Fig. 12

579　shows the comparison between the gap-filled and no gap-filled results. Obvious cloud

580　contamination is marked in the black ellipse in Fig. 12A, C. The gap-fill method used in our

581　study not only temporally interpolates the low values that are marked as cloud or aerosol

582　contaminated by the quality control layer, but also removes the noises caused by other factors.

583　Some extremely high value data (dark green dots) in Fig. 12A are also temporally smoothed,

584　as shown in Fig. 12B. The use of this gap-fill method also results in different regional GPP

585　estimates. The GPP estimate without the gap-fill method shows a total GPP of NA in 2010 as

586　13.23 Pg C, while the gap-filled method leads to an annual GPP estimation of 13.53 Pg C. In

587　addition, the GPP simulations with the gap-filled processing are more stable when conducting

588　interannual comparisons or trend analyses.

589

590
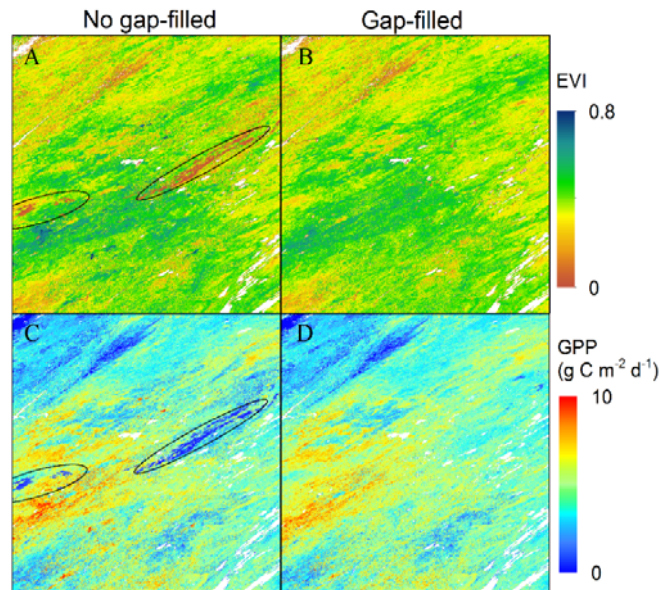
Fig. 12. Comparison between no gap-filled and gap-filled enhanced vegetation index (EVI) and the corresponding modeled gross primary production (GPP$_{VPM}$). The low value in (A) and (C) are marked out using ellipses. The scene is from the tile h11v03 during the mid-growing season on August 13th, 2010.

595

Climate data input is another potential uncertainty source for VPM simulation. Previous

studies show that VPM accurately simulates GPP at flux tower sites, when driven by *in situ*

(site-specific) meteorological data and parameters (Jin et al. 2013; Kalfas et al. 2011; Wagle et

al. 2014; Xiao et al. 2004a; Xiao et al. 2004b). As radiation is one of the direct inputs to model

GPP, the accuracy of radiation directly influences GPP simulation. Recent studies which

employ different models (MODIS PSN, EC-LUE) to investigate the performance of multiple

meteorological datasets in estimating regional GPP report that the NCEP product overestimates

radiation as compared with meteorological stations in U.S. and China (Cai et al. 2014; Zhao et

al. 2006). Jin et al. (2015) assesses the feasibility of using large scale reanalysis meteorological

data (NCEP-NARR) to drive VPM at cropland flux tower sites, and the resultant GPP$_{VPM}$

agrees well with GPP$_{EC}$ at those sites. Our validation at the site level shows that VPM

607   accurately simulates GPP across different natural biome types in NA using the regional

608   reanalysis meteorological data and biome specific parameters, suggesting that the recalibrated

609   NCEP-NARR radiation product can be used to estimate regional GPP effectively in NA.

610

611   **5. Conclusions**

612   In this study, we use VPM, climate reanalysis data, and MODIS products (vegetation

613   indices, land cover, and LST) to simulate GPP of North America. GPP_{VPM} agrees well with

614   GPP_{EC} at individual flux tower sites and the GOME-2 SIF data across North America. The

615   comparison between SIF and GPP_{VPM} showed very high spatial-temporal consistency during

616   the growing season, mostly due to the close relationship between SIF and $APAR_{chl}$. The quality

617   of GOME-2 SIF data may limit its application for evaluating the seasonal variation of GPP for

618   very low productive biome types. The results from this study clearly demonstrate the potential

619   of VPM for estimating GPP at the continental scale, and highlights the value of GOME-2 SIF

620   data for evaluation of various LUE-based and process-based GPP models. The resultant high

621   spatial and temporal resolution GPP_{VPM} dataset in North America will be provided to the public,

622   which can be further used in a wide variety of applications, especially in those studies related

623   to trend analysis, regional disturbance evaluation, model comparison, and the carbon cycle

624   under global climate change.

625

Appendix

647 Table A1

648 Biome specific lookup-table (LUT) used in the VPM model.

IGBP class	ENF[1]	EBF[2]	DNF	DBF[1]	MF[2]	CSH[2]	OSH[2]	WSA[2]	SAV[2]	GRA[2]	WET	CRO[3]	NVM
T_{min} (°C)	-1	2	-1	-1	-1	-1	1	-1	1	0	-1	-1	0
T_{opt} (°C)	20	28	20	20	19	25	31	24	30	27	20	30	27
T_{max} (°C)	40	48	40	40	48	48	48	48	48	48	40	48	48
ε_0 (g C m^{-2} day $^{-1}$ /W m^{-2})	0.078	0.078	0.078	0.078	0.078	0.078	0.078	0.078	0.078	0.078	0.078	0.108	0.078

649 ENF: evergreen needleleaf forest; EBF: evergreen broadleaf forest; DNF: deciduous needleleaf forest; DBF: deciduous broadleaf forests; MF:
650 mixed forest; CSH: closed shrublands; OSH: open shrublands; WSA: woody savannas; SAV: savannas; GRA: grassland; WET: wetland; CRO:
651 cropland; NVM: cropland/natural vegetation mosaic.
652 We use a similar temperature limitation from the Terrestrial Ecosystem Model and the T_{min}, T_{opt}, T_{max} used in this table are given by [1]Aber et
653 al. (1996) [2]McGuire et al. (1992) and [3]Wagle et al. (2015) and Kalfas et al. (2011). For some biome types (DNF, WET, NVM) which we did not
654 find reference for temperature parameters, we use parameters from similar ecosystems (e.g. ENF for DNF and WET, GRA for NVM). ε_0 for C3
655 plants are estimated from the Wagle et al. (2014), ε_0 for C4 crops is from Kalfas et al. (2011). Cropland is regarded as the half-half C3/C4
656 therefore uses an average value.

657
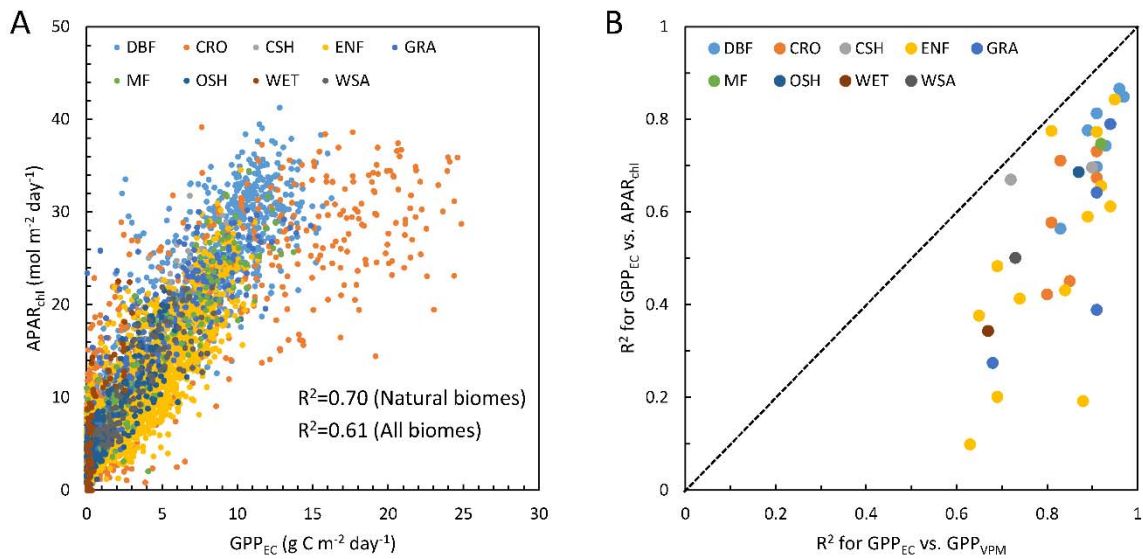
Fig. A1. (A) A comparison between GPP_{EC} and $APAR_{chl}$ for all 39 sites using 8-day data. (B)

comparison between the coefficient of determination (R^2) between GPP_{EC} vs. GPP_{VPM}, and

GPP_{EC} vs. $APAR_{chl}$ for individual sites.

References

Aber, J.D., Reich, P.B., & Goulden, M.L. (1996). Extrapolating leaf CO2 exchange to the canopy: a generalized model of forest photosynthesis compared with measurements by eddy correlation. *Oecologia, 106*, 257-265

Baker, N.R. (2008). Chlorophyll fluorescence: a probe of photosynthesis in vivo. *Annu. Rev. Plant Biol.*

Baldocchi, D. (2014). Measuring fluxes of trace gases and energy between ecosystems and the atmosphere - the state and future of the eddy covariance method. *Glob Chang Biol, 20*, 3600-3609

Baldocchi, D., Falge, E., Gu, L.H., Olson, R., Hollinger, D., Running, S., Anthoni, P., Bernhofer, C., Davis, K., Evans, R., Fuentes, J., Goldstein, A., Katul, G., Law, B., Lee, X.H., Malhi, Y., Meyers, T., Munger, W., Oechel, W., U, K.T.P., Pilegaard, K., Schmid, H.P., Valentini, R., Verma, S., Vesala, T., Wilson, K., & Wofsy, S. (2001). FLUXNET: A new tool to study the temporal and spatial variability of ecosystem-scale carbon dioxide, water vapor, and energy flux densities. *Bulletin of the American Meteorological Society, 82*, 2415-2434

Ballantyne, A.P., Alden, C.B., Miller, J.B., Tans, P.P., & White, J.W. (2012). Increase in observed net carbon dioxide uptake by land and oceans during the past 50 years. *Nature,*

681   *488*, 70-72

682 Beer, C., Reichstein, M., Tomelleri, E., Ciais, P., Jung, M., Carvalhais, N., Rödenbeck, C.,
683   Arain, M.A., Baldocchi, D., & Bonan, G.B. (2010). Terrestrial gross carbon dioxide
684   uptake: global distribution and covariation with climate. *Science, 329*, 834-838

685 Booth, B.B.B., Jones, C.D., Collins, M., Totterdell, I.J., Cox, P.M., Sitch, S., Huntingford, C.,
686   Betts, R.A., Harris, G.R., & Lloyd, J. (2012). High sensitivity of future global warming
687   to land carbon cycle processes. *Environmental Research Letters, 7*, 024002

688 Cai, W., Yuan, W., Liang, S., Zhang, X., Dong, W., Xia, J., Fu, Y., Chen, Y., Liu, D., & Zhang,
689   Q. (2014). Improved estimations of gross primary production using satellite-derived
690   photosynthetically active radiation. *Journal of Geophysical Research: Biogeosciences,*
691   *119*, 110-123

692 Chen, J., Jönsson, P., Tamura, M., Gu, Z., Matsushita, B., & Eklundh, L. (2004). A simple
693   method for reconstructing a high-quality NDVI time-series data set based on the
694   Savitzky–Golay filter. *Remote Sensing of Environment, 91*, 332-344

695 Chen, J., Yan, H., Wang, S., Gao, Y., Huang, M., Wang, J., & Xiao, X. (2014). Estimation of
696   Gross Primary Productivity in Chinese Terrestrial Ecosystems by Using VPM Model.
697   *Quaternary Sciences, 34*

698 Chen, B.Z., Coops, N.C., Fu, D., Margolis, H.A., Amiro, B.D., Black, T.A., Arain, M.A., Barr,
699   A.G., Bourque, C.P.A., Flanagan, L.B., Lafleur, P.M., McCaughey, J.H., & Wofsy, S.C.
700   (2012). Characterizing spatial representativeness of flux tower eddy-covariance
701   measurements across the Canadian Carbon Program Network using remote sensing and
702   footprint analysis. *Remote Sensing of Environment, 124*, 742-755

703 Collatz, G.J., Ribas-Carbo, M., & Berry, J.A. (1992). Coupled Photosynthesis-Stomatal
704   Conductance Model for Leaves of C4 Plants. *Australian Journal of Plant Physiology, 19*,
705   519-538

706 Cook, B.D., Davis, K.J., Wang, W.G., Desai, A., Berger, B.W., Teclaw, R.M., Martin, J.G.,
707   Bolstad, P.V., Bakwin, P.S., Yi, C.X., & Heilman, W. (2004). Carbon exchange and
708   venting anomalies in an upland deciduous forest in northern Wisconsin, USA.
709   *Agricultural and Forest Meteorology, 126*, 271-295

710 Coops, N.C., Ferster, C.J., Waring, R.H., & Nightingale, J. (2009). Comparison of three models
711   for predicting gross primary production across and within forested ecoregions in the
712   contiguous United States. *Remote Sensing of Environment, 113*, 680-690

713 Coulter, R.L., Pekour, M.S., Cook, D.R., Klazura, G.E., Martin, T.J., & Lucas, J.D. (2006).
714   Surface energy and carbon dioxide fluxes above different vegetation types within ABLE.
715   *Agricultural and Forest Meteorology, 136*, 147-158

716 Damm, A., Guanter, L., Verhoef, W., Schläpfer, D., Garbari, S., & Schaepman, M.E. (2015).
717   Impact of varying irradiance on vegetation indices and chlorophyll fluorescence derived
718   from spectroscopy data. *Remote Sensing of Environment, 156*, 202-215

719 Desai, A.R., Bolstad, P.V., Cook, B.D., Davis, K.J., & Carey, E.V. (2005). Comparing net
720   ecosystem exchange of carbon dioxide between an old-growth and mature forest in the
721   upper Midwest, USA. *Agricultural and Forest Meteorology, 128*, 33-55

722 Dijkstra, P., Hymus, G., Colavito, D., Vieglais, D.A., Cundari, C.M., Johnson, D.P., Hungate,

B.A., Hinkle, C.R., & Drake, B.G. (2002). Elevated atmospheric CO2 stimulates aboveground biomass in a fire-regenerated scrub-oak ecosystem. *Global Change Biology, 8*, 90-103

Dong, J., Xiao, X., Wagle, P., Zhang, G., Zhou, Y., Jin, C., Torn, M.S., Meyers, T.P., Suyker, A.E., Wang, J., Yan, H., Biradar, C., & Moore Iii, B. (2015a). Comparison of four EVI-based models for estimating gross primary production of maize and soybean croplands and tallgrass prairie under severe drought. *Remote Sensing of Environment, 162*, 154-168

Dong, J.W., Xiao, X.M., Kou, W.L., Qin, Y.W., Zhang, G.L., Li, L., Jin, C., Zhou, Y.T., Wang, J., Biradar, C., Liu, J.Y., & Moore, B. (2015b). Tracking the dynamics of paddy rice planting area in 1986-2010 through time series Landsat images and phenology-based algorithms. *Remote Sensing of Environment, 160*, 99-113

Dore, S., Kolb, T.E., Montes-Helu, M., Sullivan, B.W., Winslow, W.D., Hart, S.C., Kaye, J.P., Koch, G.W., & Hungate, B.A. (2008). Long-term impact of a stand-replacing fire on ecosystem CO(2) exchange of a ponderosa pine forest. *Global Change Biology, 14*, 1801-1820

Epstein, H.E., Calef, M.P., Walker, M.D., Chapin, F.S., & Starfield, A.M. (2004). Detecting changes in arctic tundra plant communities in response to warming over decadal time scales. *Global Change Biology, 10*, 1325-1334

Farquhar, G.D., Caemmerer, S.V., & Berry, J.A. (1980). A Biochemical-Model of Photosynthetic Co2 Assimilation in Leaves of C-3 Species. *Planta, 149*, 78-90

Fischer, M.L., Billesbach, D.P., Berry, J.A., Riley, W.J., & Torn, M.S. (2007). Spatiotemporal variations in growing season exchanges of CO2, H2O, and sensible heat in agricultural fields of the Southern Great Plains. *Earth Interactions, 11*

Flexas, J., Briantais, J.M., Cerovic, Z., & Medrano, H. (2000). Steady-state and maximum chlorophyll fluorescence responses to water stress in grapevine leaves: a new remote sensing system. *Remote Sensing of Environment, 73,* 283-297

Forkel, M., Carvalhais, N., Rodenbeck, C., Keeling, R., Heimann, M., Thonicke, K., Zaehle, S., & Reichstein, M. (2016). Enhanced seasonal CO2 exchange caused by amplified plant productivity in northern ecosystems. *Science, 351,* 696-699

Frankenberg, C., Fisher, J.B., Worden, J., Badgley, G., Saatchi, S.S., Lee, J.E., Toon, G.C., Butz, A., Jung, M., Kuze, A., & Yokota, T. (2011). New global observations of the terrestrial carbon cycle from GOSAT: Patterns of plant fluorescence with gross primary productivity. *Geophysical Research Letters, 38*

Frankenberg, C., O'Dell, C., Berry, J., Guanter, L., Joiner, J., Köhler, P., Pollock, R., & Taylor, T.E. (2014). Prospects for chlorophyll fluorescence remote sensing from the Orbiting Carbon Observatory-2. *Remote Sensing of Environment, 147*, 1-12

Friedl, M.A., Sulla-Menashe, D., Tan, B., Schneider, A., Ramankutty, N., Sibley, A., & Huang, X.M. (2010). MODIS Collection 5 global land cover: Algorithm refinements and characterization of new datasets. *Remote Sensing of Environment, 114*, 168-182

Gitelson, A.A., Vina, A., Verma, S.B., Rundquist, D.C., Arkebauer, T.J., Keydan, G., Leavitt, B., Ciganda, V., Burba, G.G., & Suyker, A.E. (2006). Relationship between gross primary production and chlorophyll content in crops: Implications for the synoptic monitoring of

765   vegetation productivity. *Journal of Geophysical Research-Atmospheres, 111*

766 Goldstein, A.H., Hultman, N.E., Fracheboud, J.M., Bauer, M.R., Panek, J.A., Xu, M., Qi, Y.,
767   Guenther, A.B., & Baugh, W. (2000). Effects of climate variability on the carbon dioxide,
768   water, and sensible heat fluxes above a ponderosa pine plantation in the Sierra Nevada
769   (CA). *Agricultural and Forest Meteorology, 101*, 113-129

770 Gough, C.M., Vogel, C.S., Schmid, H.P., Su, H.B., & Curtis, P.S. (2008). Multi-year
771   convergence of biometric and meteorological estimates of forest carbon storage.
772   *Agricultural and Forest Meteorology, 148*, 158-170

773 Goulden, M.L., Winston, G.C., McMillan, A.M.S., Litvak, M.E., Read, E.L., Rocha, A.V., &
774   Elliot, J.R. (2006). An eddy covariance mesonet to measure the effect of forest age on
775   land-atmosphere exchange. *Global Change Biology, 12*, 2146-2162

776 Graven, H.D., Keeling, R.F., Piper, S.C., Patra, P.K., Stephens, B.B., Wofsy, S.C., Welp, L.R.,
777   Sweeney, C., Tans, P.P., Kelley, J.J., Daube, B.C., Kort, E.A., Santoni, G.W., & Bent, J.D.
778   (2013). Enhanced seasonal exchange of CO2 by northern ecosystems since 1960. *Science,*
779   *341*, 1085-1089

780 Gray, J.M., Frolking, S., Kort, E.A., Ray, D.K., Kucharik, C.J., Ramankutty, N., & Friedl, M.A.
781   (2014). Direct human influence on atmospheric CO2 seasonality from increased cropland
782   productivity. *Nature, 515*, 398-401

783 Griffis, T.J., Baker, J.M., & Zhang, J. (2005). Seasonal dynamics and partitioning of isotopic
784   CO2 exchange in C-3/C-4 managed ecosystem. *Agricultural and Forest Meteorology,*
785   *132*, 1-19

786 Gu, L.H., Meyers, T., Pallardy, S.G., Hanson, P.J., Yang, B., Heuer, M., Hosman, K.P., Riggs,
787   J.S., Sluss, D., & Wullschleger, S.D. (2006). Direct and indirect effects of atmospheric
788   conditions and soil moisture on surface energy partitioning revealed by a prolonged
789   drought at a temperate forest site. *Journal of Geophysical Research-Atmospheres, 111*

790 Guan, K., Berry, J.A., Zhang, Y., Joiner, J., Guanter, L., Badgley, G., & Lobell, D.B. (2015).
791   Improving the monitoring of crop productivity using spaceborne solar-induced
792   fluorescence. *Glob Chang Biol,* doi: 10.1111/gcb.13136

793 Guanter, L., Aben, I., Tol, P., Krijger, J.M., Hollstein, A., Kohler, P., Damm, A., Joiner, J.,
794   Frankenberg, C., & Landgraf, J. (2015). Potential of the TROPOspheric Monitoring
795   Instrument (TROPOMI) onboard the Sentinel-5 Precursor for the monitoring of
796   terrestrial chlorophyll fluorescence. *Atmospheric Measurement Techniques, 8*, 1337-
797   1352

798 Guanter, L., Frankenberg, C., Dudhia, A., Lewis, P.E., Gomez-Dans, J., Kuze, A., Suto, H., &
799   Grainger, R.G. (2012). Retrieval and global assessment of terrestrial chlorophyll
800   fluorescence from GOSAT space measurements. *Remote Sensing of Environment, 121*,
801   236-251

802 Guanter, L., Rossini, M., Colombo, R., Meroni, M., Frankenberg, C., Lee, J.E., & Joiner, J.
803   (2013). Using field spectroscopy to assess the potential of statistical approaches for the
804   retrieval of sun-induced chlorophyll fluorescence from ground and space. *Remote*
805   *Sensing of Environment, 133*, 52-61

806 Guanter, L., Zhang, Y., Jung, M., Joiner, J., Voigt, M., Berry, J.A., Frankenberg, C., Huete,

807   A.R., Zarco-Tejada, P., Lee, J.E., Moran, M.S., Ponce-Campos, G., Beer, C., Camps-Valls,
808   G., Buchmann, N., Gianelle, D., Klumpp, K., Cescatti, A., Baker, J.M., & Griffis, T.J.
809   (2014). Global and time-resolved monitoring of crop photosynthesis with chlorophyll
810   fluorescence. *Proc Natl Acad Sci U S A, 111*, E1327-1333

811 He, H.L., Liu, M., Xiao, X.M., Ren, X.L., Zhang, L., Sun, X.M., Yang, Y.H., Li, Y.N., Zhao,
812   L., Shi, P.L., Du, M.Y., Ma, Y.M., Ma, M.G., Zhang, Y., & Yu, G.R. (2014). Large-scale
813   estimation and uncertainty analysis of gross primary production in Tibetan alpine
814   grasslands. *Journal of Geophysical Research-Biogeosciences, 119*, 466-486

815 Heinsch, F.A., Heilman, J.L., McInnes, K.J., Cobos, D.R., Zuberer, D.A., & Roelke, D.L.
816   (2004). Carbon dioxide exchange in a high marsh on the Texas Gulf Coast: effects of
817   freshwater availability. *Agricultural and Forest Meteorology, 125*, 159-172

818 Hollinger, D.Y., Aber, J., Dail, B., Davidson, E.A., Goltz, S.M., Hughes, H., Leclerc, M.Y.,
819   Lee, J.T., Richardson, A.D., Rodrigues, C., Scott, N.A., Achuatavarier, D., & Walsh, J.
820   (2004). Spatial and temporal variability in forest-atmosphere CO_2 exchange. *Global
821   Change Biology, 10*, 1689-1706

822 Hollinger, S.E., Bernacchi, C.J., & Meyers, T.P. (2005). Carbon budget of mature no-till
823   ecosystem in North Central Region of the United States. *Agricultural and Forest
824   Meteorology, 130*, 59-69

825 Huete, A., Didan, K., Miura, T., Rodriguez, E.P., Gao, X., & Ferreira, L.G. (2002). Overview
826   of the radiometric and biophysical performance of the MODIS vegetation indices.
827   *Remote Sensing of Environment, 83*, 195-213

828 Huntzinger, D.N., Post, W.M., Wei, Y., Michalak, A.M., West, T.O., Jacobson, A.R., Baker,
829   I.T., Chen, J.M., Davis, K.J., Hayes, D.J., Hoffman, F.M., Jain, A.K., Liu, S., McGuire,
830   A.D., Neilson, R.P., Potter, C., Poulter, B., Price, D., Raczka, B.M., Tian, H.Q., Thornton,
831   P., Tomelleri, E., Viovy, N., Xiao, J., Yuan, W., Zeng, N., Zhao, M., & Cook, R. (2012).
832   North American Carbon Program (NACP) regional interim synthesis: Terrestrial
833   biospheric model intercomparison. *Ecological Modelling, 232*, 144-157

834 Jenkins, J.P., Richardson, A.D., Braswell, B.H., Ollinger, S.V., Hollinger, D.Y., & Smith, M.L.
835   (2007). Refining light-use efficiency calculations for a deciduous forest canopy using
836   simultaneous tower-based carbon flux and radiometric measurements. *Agricultural and
837   Forest Meteorology, 143*, 64-79

838 Jin, C., Xiao, X., Wagle, P., Griffis, T., Dong, J., Wu, C., & Qin, Y. (2015). Effects of in-situ
839   and reanalysis climate data on estimation of cropland gross primary production using the
840   Vegetation Photosynthesis Model. *Agricultural and Forest Meteorology, 213*, 240

841 Jin, C., Xiao, X.M., Merbold, L., Arneth, A., Veenendaal, E., & Kutsch, W.L. (2013).
842   Phenology and gross primary production of two dominant savanna woodland ecosystems
843   in Southern Africa. *Remote Sensing of Environment, 135*, 189-201

844 Joiner, J., Guanter, L., Lindstrot, R., Voigt, M., Vasilkov, A.P., Middleton, E.M., Huemmrich,
845   K.F., Yoshida, Y., & Frankenberg, C. (2013). Global monitoring of terrestrial chlorophyll
846   fluorescence from moderate-spectral-resolution near-infrared satellite measurements:
847   methodology, simulations, and application to GOME-2. *Atmospheric Measurement
848   Techniques, 6*, 2803-2823

849 Joiner, J., Yoshida, Y., Vasilkov, A.P., Middleton, E.M., Campbell, P.K.E., Yoshida, Y., Kuze,
850   A., & Corp, L.A. (2012). Filling-in of near-infrared solar lines by terrestrial fluorescence
851   and other geophysical effects: simulations and space-based observations from
852   SCIAMACHY and GOSAT. *Atmospheric Measurement Techniques, 5*, 809-829

853 Joiner, J., Yoshida, Y., Vasilkov, A.P., Schaefer, K., Jung, M., Guanter, L., Zhang, Y., Garrity,
854   S., Middleton, E.M., Huemmrich, K.F., Gu, L., & Belelli Marchesini, L. (2014). The
855   seasonal cycle of satellite chlorophyll fluorescence observations and its relationship to
856   vegetation phenology and ecosystem atmosphere carbon exchange. *Remote Sensing of
857   Environment, 152*, 375-391

858 Joiner, J., Yoshida, Y., Vasilkov, A.P., Yoshida, Y., Corp, L.A., & Middleton, E.M. (2011). First
859   observations of global and seasonal terrestrial chlorophyll fluorescence from space.
860   *Biogeosciences, 8*, 637-651

861 Jung, M., Reichstein, M., & Bondeau, A. (2009). Towards global empirical upscaling of
862   FLUXNET eddy covariance observations: validation of a model tree ensemble approach
863   using a biosphere model. *Biogeosciences, 6*, 2001-2013

864 Jung, M., Reichstein, M., Margolis, H.A., Cescatti, A., Richardson, A.D., Arain, M.A., Arneth,
865   A., Bernhofer, C., Bonal, D., Chen, J.Q., Gianelle, D., Gobron, N., Kiely, G., Kutsch, W.,
866   Lasslop, G., Law, B.E., Lindroth, A., Merbold, L., Montagnani, L., Moors, E.J., Papale,
867   D., Sottocornola, M., Vaccari, F., & Williams, C. (2011). Global patterns of land-
868   atmosphere fluxes of carbon dioxide, latent heat, and sensible heat derived from eddy
869   covariance, satellite, and meteorological observations. *Journal of Geophysical Research-
870   Biogeosciences, 116*

871 Kalfas, J.L., Xiao, X., Vanegas, D.X., Verma, S.B., & Suyker, A.E. (2011). Modeling gross
872   primary production of irrigated and rain-fed maize using MODIS imagery and CO2 flux
873   tower data. *Agricultural and Forest Meteorology, 151*, 1514-1528

874 Keenan, T.F., Baker, I., Barr, A., Ciais, P., Davis, K., Dietze, M., Dragoni, D., Gough, C.M.,
875   Grant, R., Hollinger, D., Hufkens, K., Poulter, B., McCaughey, H., Raczka, B., Ryu, Y.,
876   Schaefer, K., Tian, H., Verbeeck, H., Zhao, M., & Richardson, A.D. (2012). Terrestrial
877   biosphere model performance for inter-annual variability of land-atmosphere CO2
878   exchange. *Global Change Biology, 18*, 1971-1987

879 Kraft, S., Bézy, J.L., Del Bello, U., Berlich, R., Drusch, M., Franco, R., Gabriele, A., Harnisch,
880   B., Meynart, R., & Silvestrin, P. (2013). FLORIS: phase A status of the fluorescence
881   imaging spectrometer of the Earth Explorer mission candidate FLEX. Proc. SPIE 8889,
882   Sensors, Systems, and Next-Generation Satellites XVII, 8889, 88890T-88812

883 Krinner, G., Viovy, N., de Noblet-Ducoudre, N., Ogee, J., Polcher, J., Friedlingstein, P., Ciais,
884   P., Sitch, S., & Prentice, I.C. (2005). A dynamic global vegetation model for studies of
885   the coupled atmosphere-biosphere system. *Global Biogeochemical Cycles, 19*

886 Law, B.E., Turner, D., Campbell, J., Sun, O.J., Van Tuyl, S., Ritts, W.D., & Cohen, W.B. (2004).
887   Disturbance and climate effects on carbon stocks and fluxes across Western Oregon USA.
888   *Global Change Biology, 10*, 1429-1444

889 Law, B.E., Williams, M., Anthoni, P.M., Baldocchi, D.D., & Unsworth, M.H. (2000).
890   Measuring and modelling seasonal variation of carbon dioxide and water vapour

exchange of a Pinus ponderosa forest subject to soil water deficit. *Global Change Biology, 6*, 613-630

Lee, J.E., Berry, J.A., van der Tol, C., Yang, X., Guanter, L., Damm, A., Baker, I., & Frankenberg, C. (2015). Simulations of chlorophyll fluorescence incorporated into the Community Land Model version 4. *Glob Chang Biol, 21,* 3469–3477, doi: 10.1111/gcb.12948

Luo, Y.Q., Randerson, J.T., Abramowitz, G., Bacour, C., Blyth, E., Carvalhais, N., Ciais, P., Dalmonech, D., Fisher, J.B., Fisher, R., Friedlingstein, P., Hibbard, K., Hoffman, F., Huntzinger, D., Jones, C.D., Koven, C., Lawrence, D., Li, D.J., Mahecha, M., Niu, S.L., Norby, R., Piao, S.L., Qi, X., Peylin, P., Prentice, I.C., Riley, W., Reichstein, M., Schwalm, C., Wang, Y.P., Xia, J.Y., Zaehle, S., & Zhou, X.H. (2012). A framework for benchmarking land models. *Biogeosciences*, *9*, 3857-3874

Ma, S.Y., Baldocchi, D.D., Xu, L.K., & Hehn, T. (2007). Inter-annual variability in carbon dioxide exchange of an oak/grass savanna and open grassland in California. *Agricultural and Forest Meteorology, 147*, 157-171

McGuire, A.D., Melillo, J., Joyce, L., Kicklighter, D., Grace, A., Moore, B., & Vorosmarty, C. (1992). Interactions between carbon and nitrogen dynamics in estimating net primary productivity for potential vegetation in North America. *Global Biogeochemical Cycles, 6*, 101-124

Mesinger, F., DiMego, G., Kalnay, E., Mitchell, K., Shafran, P.C., Ebisuzaki, W., Jovic, D., Woollen, J., Rogers, E., Berbery, E.H., Ek, M.B., Fan, Y., Grumbine, R., Higgins, W., Li, H., Lin, Y., Manikin, G., Parrish, D., & Shi, W. (2006). North American regional reanalysis. *Bulletin of the American Meteorological Society, 87*, 343-+

Monteith, J.L. (1972). Solar-Radiation and Productivity in Tropical Ecosystems. *Journal of Applied Ecology, 9*, 747-766

Noormets, A., Gavazzi, M.J., Mcnulty, S.G., Domec, J.C., Sun, G., King, J.S., & Chen, J.Q. (2010). Response of carbon fluxes to drought in a coastal plain loblolly pine forest. *Global Change Biology, 16*, 272-287

Parazoo, N.C., Bowman, K., Fisher, J.B., Frankenberg, C., Jones, D.B., Cescatti, A., Perez-Priego, O., Wohlfahrt, G., & Montagnani, L. (2014). Terrestrial gross primary production inferred from satellite fluorescence and vegetation models. *Glob Chang Biol, 20*, 3103-3121

Piao, S., Sitch, S., Ciais, P., Friedlingstein, P., Peylin, P., Wang, X., Ahlstrom, A., Anav, A., Canadell, J.G., Cong, N., Huntingford, C., Jung, M., Levis, S., Levy, P.E., Li, J., Lin, X., Lomas, M.R., Lu, M., Luo, Y., Ma, Y., Myneni, R.B., Poulter, B., Sun, Z., Wang, T., Viovy, N., Zaehle, S., & Zeng, N. (2013). Evaluation of terrestrial carbon cycle models for their response to climate variability and to CO2 trends. *Glob Chang Biol, 19*, 2117-2132

Porcar-Castell, A., Bäck, J., Juurola, E., & Hari, P. (2006). Dynamics of the energy flow through photosystem II under changing light conditions: a model approach. *Functional plant biology*

Porcar-Castell, A., Tyystjarvi, E., Atherton, J., van der Tol, C., Flexas, J., Pfundel, E.E., Moreno,

J., Frankenberg, C., & Berry, J.A. (2014). Linking chlorophyll a fluorescence to photosynthesis for remote sensing applications: mechanisms and challenges. *Journal of experimental Botany, 65*, 4065-4095

Potter, C.S., Randerson, J.T., Field, C.B., Matson, P.A., Vitousek, P.M., Mooney, H.A., & Klooster, S.A. (1993). Terrestrial Ecosystem Production - a Process Model-Based on Global Satellite and Surface Data. *Global Biogeochemical Cycles, 7*, 811-841

Poulter, B., Frank, D., Ciais, P., Myneni, R.B., Andela, N., Bi, J., Broquet, G., Canadell, J.G., Chevallier, F., Liu, Y.Y., Running, S.W., Sitch, S., & van der Werf, G.R. (2014). Contribution of semi-arid ecosystems to interannual variability of the global carbon cycle. *Nature, 509*, 600-603

Raich, J., Rastetter, E., Melillo, J., Kicklighter, D., Steudler, P., Peterson, B., Grace, A., Moore Iii, B., & Vorosmarty, C. (1991). Potential net primary productivity in South America: application of a global model. *Ecological Applications, 1*, 399-429

Reichstein, M., Falge, E., Baldocchi, D., Papale, D., Aubinet, M., Berbigier, P., Bernhofer, C., Buchmann, N., Gilmanov, T., Granier, A., Grunwald, T., Havrankova, K., Ilvesniemi, H., Janous, D., Knohl, A., Laurila, T., Lohila, A., Loustau, D., Matteucci, G., Meyers, T., Miglietta, F., Ourcival, J.-M., Pumpanen, J., Rambal, S., Rotenberg, E., Sanz, M., Tenhunen, J., Seufert, G., Vaccari, F., Vesala, T., Yakir, D., & Valentini, R. (2005). On the separation of net ecosystem exchange into assimilation and ecosystem respiration: review and improved algorithm. *Global Change Biology, 11*, 1424-1439

Rossini, M., Nedbal, L., Guanter, L., Ač, A., Alonso, L., Burkart, A., Cogliati, S., Colombo, R., Damm, A., Drusch, M., Hanus, J., Janoutova, R., Julitta, T., Kokkalis, P., Moreno, J., Novotny, J., Panigada, C., Pinto, F., Schickling, A., Schüttemeyer, D., Zemek, F., & Rascher, U. (2015). Red and far-red sun-induced chlorophyll fluorescence as a measure of plant photosynthesis. *Geophysical Research Letters*, n/a-n/a

Running, S.W., Nemani, R.R., Heinsch, F.A., Zhao, M.S., Reeves, M., & Hashimoto, H. (2004). A continuous satellite-derived measure of global terrestrial primary production. *Bioscience, 54*, 547-560

Schmid, H.P., Grimmond, C.S.B., Cropley, F., Offerle, B., & Su, H.B. (2000). Measurements of CO2 and energy fluxes over a mixed hardwood forest in the mid-western United States. *Agricultural and Forest Meteorology, 103*, 357-374

Sitch, S., Smith, B., Prentice, I.C., Arneth, A., Bondeau, A., Cramer, W., Kaplan, J.O., Levis, S., Lucht, W., Sykes, M.T., Thonicke, K., & Venevsky, S. (2003). Evaluation of ecosystem dynamics, plant geography and terrestrial carbon cycling in the LPJ dynamic global vegetation model. *Global Change Biology, 9*, 161-185

Sitch, S., Huntingford, C., Gedney, N., Levy, P.E., Lomas, M., Piao, S.L., Betts, R., Ciais, P., Cox, P., Friedlingstein, P., Jones, C.D., Prentice, I.C., & Woodward, F.I. (2008). Evaluation of the terrestrial carbon cycle, future plant geography and climate-carbon cycle feedbacks using five Dynamic Global Vegetation Models (DGVMs). *Glob Chang Biol, 14*, 2015-2039

Smith, B., Prentice, I.C., & Sykes, M.T. (2001). Representation of vegetation dynamics in the modelling of terrestrial ecosystems: comparing two contrasting approaches within

975 European climate space. *Global Ecology and Biogeography, 10*, 621-637

976 Soukupová, J., Cséfalvay, L., Urban, O., & Košvancová, M. (2008). Annual variation of the

977 steady-state chlorophyll fluorescence emission of evergreen plants in temperate zone.

978 *Functional Plant ...*

979 Sulman, B.N., Desai, A.R., Cook, B.D., Saliendra, N., & Mackay, D.S. (2009). Contrasting

980 carbon dioxide fluxes between a drying shrub wetland in Northern Wisconsin, USA, and

981 nearby forests. *Biogeosciences, 6*, 1115-1126

982 Sun, G., Noormets, A., Chen, J., & McNulty, S.G. (2008). Evapotranspiration estimates from

983 eddy covariance towers and hydrologic modeling in managed forests in Northern

984 Wisconsin, USA. *Agricultural and Forest Meteorology, 148*, 257-267

985 Suyker, A.E., Verma, S.B., Burba, G.G., & Arkebauer, T.J. (2005). Gross primary production

986 and ecosystem respiration of irrigated maize and irrigated soybean during a growing

987 season. *Agricultural and Forest Meteorology, 131*, 180-190

988 Urbanski, S., Barford, C., Wofsy, S., Kucharik, C., Pyle, E., Budney, J., McKain, K., Fitzjarrald,

989 D., Czikowsky, M., & Munger, J.W. (2007). Factors controlling CO_2 exchange on

990 timescales from hourly to decadal at Harvard Forest. *Journal of Geophysical Research-*

991 *Biogeosciences, 112*

992 Vanderhoof, M., Williams, C., Pasay, M., & Ghimire, B. (2013). Controls on the rate of CO_2

993 emission from woody debris in clearcut and coniferous forest environments.

994 *Biogeochemistry, 114*, 299-311

995 Verrelst, J., Rivera, J.P., van der Tol, C., Magnani, F., Mohammed, G., & Moreno, J. (2015).

996 Global sensitivity analysis of the SCOPE model: What drives simulated canopy-leaving

997 sun-induced fluorescence? *Remote Sensing of Environment, 166*, 8-21

998 Wagle, P., Xiao, X., Torn, M.S., Cook, D.R., Matamala, R., Fischer, M.L., Jin, C., Dong, J., &

999 Biradar, C. (2014). Sensitivity of vegetation indices and gross primary production of

1000 tallgrass prairie to severe drought. *Remote Sensing of Environment, 152*, 1-14

1001 Wagle, P., Xiao, X.M., & Suyker, A.E. (2015). Estimation and analysis of gross primary

1002 production of soybean under various management practices and drought conditions.

1003 *ISPRS Journal of Photogrammetry and Remote Sensing, 99*, 70-83

1004 Wagle, P., Zhang, Y., Jin, C., & Xiao, X. (2016). Comparison of solar-induced chlorophyll

1005 fluorescence, light-use efficiency, and process-based GPP models in maize. *Ecological*

1006 *Applications.* doi: 10.1890/15-1434.1

1007 Wilson, T.B., & Meyers, T.P. (2007). Determining vegetation indices from solar and

1008 photosynthetically active radiation fluxes. *Agricultural and Forest Meteorology, 144*,

1009 160-179

1010 Wu, C.Y., Munger, J.W., Niu, Z., & Kuang, D. (2010a). Comparison of multiple models for

1011 estimating gross primary production using MODIS and eddy covariance data in Harvard

1012 Forest. *Remote Sensing of Environment, 114*, 2925-2939

1013 Wu, C.Y., Niu, Z., & Gao, S.A. (2010b). Gross primary production estimation from MODIS

1014 data with vegetation index and photosynthetically active radiation in maize. *Journal of*

1015 *Geophysical Research-Atmospheres, 115*

1016 Xia, J., Chen, J., Piao, S., Ciais, P., Luo, Y., & Wan, S. (2014). Terrestrial carbon cycle affected

by non-uniform climate warming. *Nature Geoscience, 7*, 173-180

Xiao, J., Zhuang, Q., Law, B.E., Chen, J., Baldocchi, D.D., Cook, D.R., Oren, R., Richardson, A.D., Wharton, S., & Ma, S. (2010). A continuous measure of gross primary production for the conterminous United States derived from MODIS and AmeriFlux data. *Remote Sensing of Environment, 114*, 576-591

Xiao, J.F., Ollinger, S.V., Frolking, S., Hurtt, G.C., Hollinger, D.Y., Davis, K.J., Pan, Y.D., Zhang, X.Y., Deng, F., Chen, J.Q., Baldocchi, D.D., Law, B.E., Arain, M.A., Desai, A.R., Richardson, A.D., Sun, G., Amiro, B., Margolis, H., Gu, L.H., Scott, R.L., Blanken, P.D., & Suyker, A.E. (2014). Data-driven diagnostics of terrestrial carbon dynamics over North America. *Agricultural and Forest Meteorology, 197*, 142-157

Xiao, X., Boles, S., Liu, J., Zhuang, D., & Liu, M. (2002). Characterization of forest types in Northeastern China, using multi-temporal SPOT-4 VEGETATION sensor data. *Remote Sensing of Environment, 82*, 335-348

Xiao, X., Hollinger, D., Aber, J., Goltz, M., Davidson, E.A., Zhang, Q., & Moore, B. (2004a). Satellite-based modeling of gross primary production in an evergreen needleleaf forest. *Remote Sensing of Environment, 89*, 519-534

Xiao, X., Zhang, Q., Braswell, B., Urbanski, S., Boles, S., Wofsy, S., Moore, B., & Ojima, D. (2004b). Modeling gross primary production of temperate deciduous broadleaf forest using satellite images and climate data. *Remote Sensing of Environment, 91*, 256-270

Xiao, X.M., Zhang, Q.Y., Saleska, S., Hutyra, L., De Camargo, P., Wofsy, S., Frolking, S., Boles, S., Keller, M., & Moore, B. (2005). Satellite-based modeling of gross primary production in a seasonally moist tropical evergreen forest. *Remote Sensing of Environment, 94*, 105-122

Xu, L.K., & Baldocchi, D.D. (2004). Seasonal variation in carbon dioxide exchange over a Mediterranean annual grassland in California. *Agricultural and Forest Meteorology, 123*, 79-96

Yang, F.H., Ichii, K., White, M.A., Hashimoto, H., Michaelis, A.R., Votava, P., Zhu, A.X., Huete, A., Running, S.W., & Nemani, R.R. (2007). Developing a continental-scale measure of gross primary production by combining MODIS and AmeriFlux data through Support Vector Machine approach. *Remote Sensing of Environment, 110*, 109-122

Yang, X., Tang, J., Mustard, J.F., Lee, J.-E., Rossini, M., Joiner, J., Munger, J.W., Kornfeld, A., & Richardson, A.D. (2015). Solar-induced chlorophyll fluorescence correlates with canopy photosynthesis on diurnal and seasonal scales in a temperate deciduous forest. *Geophysical Research Letters*, n/a-n/a

Yu, G.R., Zhu, X.J., Fu, Y.L., He, H.L., Wang, Q.F., Wen, X.F., Li, X.R., Zhang, L.M., Zhang, L., Su, W., Li, S.G., Sun, X.M., Zhang, Y.P., Zhang, J.H., Yan, J.H., Wang, H.M., Zhou, G.S., Jia, B.R., Xiang, W.H., Li, Y.N., Zhao, L., Wang, Y.F., Shi, P.L., Chen, S.P., Xin, X.P., Zhao, F.H., Wang, Y.Y., & Tong, C.L. (2013). Spatial patterns and climate drivers of carbon fluxes in terrestrial ecosystems of China. *Global Change Biology, 19*, 798-810

Yuan, W., Cai, W., Xia, J., Chen, J., Liu, S., Dong, W., Merbold, L., Law, B., Arain, A., Beringer, J., Bernhofer, C., Black, A., Blanken, P.D., Cescatti, A., Chen, Y., Francois, L., Gianelle, D., Janssens, I.A., Jung, M., Kato, T., Kiely, G., Liu, D., Marcolla, B., Montagnani, L.,

Raschi, A., Roupsard, O., Varlagin, A., & Wohlfahrt, G. (2014). Global comparison of light use efficiency models for simulating terrestrial vegetation gross primary production based on the LaThuile database. *Agricultural and Forest Meteorology, 192-193*, 108-120

Yuan, W., Liu, S., Zhou, G., Zhou, G., Tieszen, L.L., Baldocchi, D., Bernhofer, C., Gholz, H., Goldstein, A.H., Goulden, M.L., Hollinger, D.Y., Hu, Y., Law, B.E., Stoy, P.C., Vesala, T., & Wofsy, S.C. (2007). Deriving a light use efficiency model from eddy covariance flux data for predicting daily gross primary production across biomes. *Agricultural and Forest Meteorology, 143*, 189-207

Zeng, N., Mariotti, A., & Wetzel, P. (2005). Terrestrial mechanisms of interannual CO(2) variability. *Global Biogeochemical Cycles, 19*

Zeng, N., Zhao, F., Collatz, G.J., Kalnay, E., Salawitch, R.J., West, T.O., & Guanter, L. (2014). Agricultural Green Revolution as a driver of increasing atmospheric CO2 seasonal amplitude. *Nature, 515*, 394-397

Zhang, G., Xiao, X., Dong, J., Kou, W., Jin, C., Qin, Y., Zhou, Y., Wang, J., Menarguez, M.A., & Biradar, C. (2015). Mapping paddy rice planting areas through time series analysis of MODIS land surface temperature and vegetation index data. *ISPRS Journal of Photogrammetry and Remote Sensing, 106*, 157-171

Zhang, Y., Guanter, L., Berry, J.A., Joiner, J., van der Tol, C., Huete, A., Gitelson, A., Voigt, M., & Kohler, P. (2014). Estimation of vegetation photosynthetic capacity from space-based measurements of chlorophyll fluorescence for terrestrial biosphere models. *Glob Chang Biol, 20*, 3727-3742

Zhang, Y., Xiao, X., Zhou, S., Ciais, P., McCarthy, H., & Luo, Y. (2016). Canopy and physiological controls of GPP during drought and heat wave. *Geophysical Research Letters, 43*, 3325-3333

Zhao, M., Heinsch, F.A., Nemani, R.R., & Running, S.W. (2005). Improvements of the MODIS terrestrial gross and net primary production global data set. *Remote Sensing of Environment, 95*, 164-176

Zhao, M., Running, S.W., & Nemani, R.R. (2006). Sensitivity of Moderate Resolution Imaging Spectroradiometer (MODIS) terrestrial primary production to the accuracy of meteorological reanalyses. *Journal of Geophysical Research-Biogeosciences, 111*